

## Stellar Halo Morphology from TNG50: Twisted and Twisted-Stretched Halos

RAZIEH EMAMI,<sup>1</sup> LARS HERNQUIST,<sup>1</sup> CHARLES ALCOCK,<sup>1</sup> SHY GENEL,<sup>2,3</sup> SOWNAK BOSE,<sup>1</sup> RAINER WEINBERGER,<sup>1</sup>  
MARK VOGELSBERGER,<sup>4</sup> XUEJIAN SHEN,<sup>5</sup> JOSHUA S. SPEAGLE,<sup>6,7,8,\*</sup> FEDERICO MARINACCI,<sup>9</sup> JOHN C. FORBES,<sup>2</sup> AND  
PAUL TORREY<sup>10</sup>

<sup>1</sup>*Center for Astrophysics | Harvard & Smithsonian, 60 Garden Street, Cambridge, MA 02138, USA*

<sup>2</sup>*Center for Computational Astrophysics, Flatiron Institute, New York, USA*

<sup>3</sup>*Columbia Astrophysics Laboratory, Columbia University, 550 West 120th Street, New York, NY 10027, USA*

<sup>4</sup>*Department of Physics, Kavli Institute for Astrophysics and Space Research, Massachusetts Institute of Technology, Cambridge, MA 02139, USA*

<sup>5</sup>*TAPIR, California Institute of Technology, Pasadena, CA 91125, USA*

<sup>6</sup>*Department of Statistical Sciences, University of Toronto, Toronto, M5S 3G3, Canada*

<sup>7</sup>*Dunlap Institute for Astronomy & Astrophysics, University of Toronto, Toronto, M5S 3H4, Canada*

<sup>8</sup>*David A. Dunlap Department of Astronomy & Astrophysics, University of Toronto, Toronto, M5S 3H4, Canada*

<sup>9</sup>*Department of Physics & Astronomy "Augusto Righi", University of Bologna, via Gobetti 93/2, 40129 Bologna, Italy*

<sup>10</sup>*Department of Astronomy, University of Florida, 211 Bryant Space Sciences Center, Gainesville, FL 32611, USA*

(Received; Revised; Accepted)

Submitted to ApJ

### ABSTRACT

We investigate the morphology of the stellar halo (SH) in a sample of Milky Way (MW) like galaxies in the TNG50 simulation. Using a local in shell iterative method (LSIM) as the main approach, we explicitly show evidence of twisting (in about 52% of halos) and stretching (in 48% of them) in the real space. This is matched with the re-orientation observed in the eigenvectors of the inertia tensor and gives us a clear picture of having a re-oriented SH. We make a comparison between the shape profile of dark matter (DM) halo and SH and quite remarkably see that their radial profiles are fairly close, especially at small galactocentric radii where the stellar disk is located. This implies that the DM halo is somewhat aligned with the stellar disk in response to the baryonic potential. The level of alignment mostly decreases away from the center. We study the impact of substructures in the orbital circularity parameter. It is demonstrated that in some halos far away substructures are counter-rotating compared with the central stars and may flip the sign of total angular momentum and thus the orbital circularity parameter. Truncating them above 150 kpc, however, retains the disk structure of the galaxy as per initial selection. Including the impact of substructures in the shape of SH, we explicitly show that their contribution is subdominant. Overlaying our theoretical results to the observational constraints from previous literature, we establish a fair agreement.

*Keywords:* TNG Simulation, Milky Way Galaxy, Stellar halo, Morphology

### 1. INTRODUCTION

According to the standard paradigm of galaxy formation, galaxies are formed hierarchically and in multiple phases, where the early formation phase involves the col-

lapse of gas and in-situ star formation, while the latter phase includes the accretion and merger of many smaller structures forming the stellar halo (SH) (White & Rees 1978; Searle & Zinn 1978; Blumenthal et al. 1984; White & Frenk 1991; Navarro et al. 1997; Forbes et al. 1997; Oser et al. 2010; Beasley et al. 2018). Such accreted structures, lead to the formation of tidal debris in different stages of the phase mixing. Consequently, the stellar halo is expected to retain information regarding to the

Corresponding author: Razieh Emami  
razieh.emami\_meibody@cfa.harvard.edu

\* Banting Fellow

assembly history of the galaxy and can be treated as a direct tracer of the galaxy morphology and evolution.

Observations of the Milky Way (MW), reveal that MW has encountered multiple phases of accretions as a build up of its stellar halo (Ibata et al. 1994; Helmi & White 1999; Helmi et al. 2018; Mackereth & Bovy 2020; Naidu et al. 2020). Such accreted structures complicate observational measurements of the morphology of galaxies. Indeed, there have been many extensive endeavors to measure the shape of the stellar halo in the MW galaxy in real space (Vivas & Zinn 2006; Ivezić et al. 2008; Bell et al. 2008; Watkins et al. 2009; Sesar et al. 2010; Deason et al. 2011; Sesar et al. 2013; Belokurov et al. 2014; Faccioli et al. 2014; Iorio & Belokurov 2019; Kado-Fong et al. 2020) using different stellar types, such as blue horizontal branch (BHB) and blue straggler (BS) stars (Deason et al. 2011), main sequence turnoff (MSTO) stars (Bell et al. 2008) and RR Lyrae stars (RRLS) (Sesar et al. 2013; Iorio & Belokurov 2019), as tracers. Or in velocity space, in terms of the velocity anisotropy (Myeong et al. 2019; Bird et al. 2020; Iorio & Belokurov 2020). However, owing to the aforementioned complexities as well as the very non-trivial selection functions for the surveys, not all of such observational studies lead to the same final results.

As a result, there have been many attempts to model the galaxy morphology traced either by the DM or SH halos, theoretically. In the last decade, there have been many improvements in the study of the morphology of galaxies using hydrodynamical simulations like EAGLE (Schaye et al. 2015; Crain et al. 2015; Trayford et al. 2019; Font et al. 2020), AURIGA (Monachesi et al. 2016; Grand et al. 2018; Hani et al. 2019), NIHAO-UHD (Buck et al. 2018, 2020) and FIRE-2 (Garrison-Kimmel et al. 2018; El-Badry et al. 2018; Orr et al. 2019; Sanderson et al. 2020; Santistevan et al. 2020). Added to the above list, there have been also quite some investigations using the Illustris simulation (Vogelsberger et al. 2014a,b; Genel et al. 2014; Sijacki et al. 2015) and IllustrisTNG simulations (Naiman et al. 2018; Pillepich et al. 2018; Springel et al. 2018; Nelson et al. 2018; Marinacci et al. 2018; Vogelsberger et al. 2020; Merritt et al. 2020).

Perhaps the best advantage of using cosmological hydrodynamical simulations is the capability to disentangle between the contribution of the central halo and the substructures on the stellar morphology, to get rid of the selection biases and to quantify the impact of using different tracers to probe stellar halo shape. It is very common to either use the dark matter (DM) or SH as different tracers in probing the galaxy morphology. In Emami et al. (2020), we used the TNG50 simulation (Pillepich et al. 2019; Nelson et al. 2019), the highest res-

olution from the series of IllustrisTNG simulations, and investigated the shape of a sample of MW like galaxies using the DM as the tracer. We explicitly showed that the DM halo in TNG galaxies is consistent with a triaxial shape and provided evidence for both gradual and abrupt rotations of the DM halo. Since DM gives us an indirect estimate of the galaxy morphology, it is essential to calculate the galaxy morphology using the stellar halo and compare that with the estimated shape from the DM halo. This is rather essential as measuring the level of rotation in the DM is extremely hard, if not impossible. On the contrary, modeling galaxy morphology using the stellar halo potentially enables us to check how we could measure them using spectroscopic surveys in our Galaxy.

Motivated by this, in the current paper, we analyze the galaxy shape using the stellar halo. We analyse the shape both from the statistical perspective as well as individual halos. In the latter case, we make some classifications for the shape of the stellar halos, putting them into two main classes: twisted and twisted-stretched halos. We report some levels of gradual or rather abrupt rotation for different halos in our sample. In addition, we make a comparison between the morphology of the DM halos (Emami et al. 2020), and the current analysis, for which we use the results of our various algorithms. Although the details of such comparison depend on the method we use, our analysis explicitly shows that in some sense DM and stellar halos are fairly similar. We study the impact of gravitationally self-bound substructures on the shape of stellar halo and very remarkably demonstrate that in most cases, their impact is subdominant. Finally, we overlay our theoretical results on top of recent observational measurements and establish a rather fair agreement between the two.

The paper is structured as follows. In Sec. 2, we review the simulation setup and the sample selection. Sec. 3 presents several different methods to compute the SH halo shape. Sec. 4 focuses on analysing the shape profiles. In Sec. 5, we explicitly compare the shape of the DM and stellar halo. Sec. 6, we study the impact of the substructures in the shape analysis. In Sec. 7, we make the comparison between our theoretical results and the observational outcome from previous literature. We present few technical details on the halo classes in Appendix A.

## 2. SAMPLE OF MW LIKE GALAXIES IN TNG SIMULATION

Below, we present a short summary about the TNG50 simulation (Pillepich et al. 2019; Nelson et al. 2019) as

well as our sample selections in a similar way to [Emami et al. \(2020\)](#).

### 2.1. TNG50 Simulation

TNG50 is the highest resolution of the IllustrisTNG cosmological hydrodynamical simulations ([Pillepich et al. 2019](#); [Nelson et al. 2019](#)). Table 1 describes the parameters of the model and its mass and gravitational force resolution. The simulation contains different components, such as the DM, gas, stars, supermassive black holes (SMBHs) and magnetic fields which are self consistently evolved with time in a periodic box. More explicitly, starting from  $z = 127$  and using the Zelovich approximation to generate the initial condition, the system was evolved in time using the AREPO code ([Springel 2010](#)) and by solving a set of coupled differential equations for magnetohydrodynamics (MHD) and self-gravity. The latter is treated numerically by using a tree-particle-mesh algorithm ([Springel 2010](#)). In the last column of each row, we present the softeninglength for DM/stars. It is taken as 0.39 comoving kpc/h for redshifts above unity and gets lower down to 0.195 comoving kpc/h at lower redshifts.

The cosmological parameters are chosen from [Planck Collaboration et al. \(2016\)](#), with the values,  $\Omega_b = 0.0486$ ,  $\Omega_m = \Omega_{dm} + \Omega_b = 0.3089$ ,  $\Omega_\Lambda = 0.6911$ ,  $h = 0.6774$ ,  $H_0 = 100h\text{kms}^{-1}\text{Mpc}^{-1}$ ,  $\sigma_8 = 0.8159$  and  $n_s = 0.9667$ .

On the other hand, the unresolved astrophysical processes which are used in TNG50, like star formation, stellar feedback and SMBH formation, growth and the feedback are similar to IllustrisTNG simulations with the main differences in: (i) the feedback and growth of SMBH, where in the TNG simulation BH driven winds are produced through an AGN feedback model. (ii) In the galactic winds, where unlike the IllustrisTNG, the wind particles are isotropic as they are assigned an initial velocity pointed in a random directions. (iii) In the stellar evolution and the gas chemical enrichment, in which the stellar evolution is tracked through 3 main stellar phases: from the asymptotic giant branch (AGB) stars (in the mass range 1-8  $M_\odot$ ); or through the core-collapse supernovae (SNII) and from the supernovae type Ia (SNIa) (both in the range 8-100  $M_\odot$ ). See [Weinberger et al. \(2017\)](#); [Pillepich et al. \(2018\)](#) for more details on the TNG model.

### 2.2. MW like galaxies in TNG50

As it is described below, throughout our analysis in this paper, we study a sample of 25 Milky Way (MW) like galaxies with the following common features. On one hand, we propose the DM part of subhalo masses

to be restricted in the mass range  $(1 - 1.6) \times 10^{12} M_\odot$ , consistent with recent estimates of the MW mass ([Posti & Helmi 2019](#)). This brings us a total number of 71 galaxies in the above mass range. On the other hand, we require them all to have disk-like, rotationally-supported morphologies. Where by disk-like morphology, we mean galaxies which are rotationally supported. This was confirmed observationally that, based on that observationally, galaxies in the local universe, such as the MW, show a manifestly disk-like morphology ([Schinnerer et al. 2013](#)). Below, we summarize our algorithm, following [Abadi et al. \(2003\)](#); [El-Badry et al. \(2018\)](#), to identify the disk-like galaxies.

#### 2.2.1. Orbital circularity parameter

As already mentioned above, throughout our analysis, we are only interested in the rotationally supported MW like galaxies. The rotational support is measured using the orbital circularity parameter,  $\varepsilon$ , which describes the level of the alignment between the angular momentum of the individual stars and the net specific angular momentum of the galaxy:

$$\mathbf{j}_{\text{net}} \equiv \frac{\mathbf{J}_{\text{tot}}}{M} = \frac{\sum_i m_i \mathbf{r}_i \times \mathbf{v}_i}{\sum_i m_i}, \quad (1)$$

where  $i$  refers to the star particles and the sum is performed for all star particles belonging to the simulated galaxy. Pointing the  $z$  axis along with the  $\mathbf{j}_{\text{net}}$  direction, we compute the inner product of the angular momentum of individual stars and  $z$  axis,  $j_{z,i} = \mathbf{j}_i \cdot \hat{\mathbf{z}}$ . The orbital circularity parameter is then defined as:

$$\varepsilon_i \equiv \frac{j_{z,i}}{j_c(E_i)}, \quad j_c(E_i) = r_c v_c = \sqrt{GM(\leq r_c)r_c}. \quad (2)$$

where  $j_c(E_i)$  describes the specific angular momentum of the  $i$ -th stellar particle rotating in a circular orbit, which is specified with the radius  $r_c$  and energy  $E_i$  (see [Emami et al. \(2020\)](#) for more details).

Disk stars are determined as those with  $\varepsilon_i \geq 0.7$ . Furthermore, we limit our sample to cases where more than 40% of the stars that are in a radial distance less than 10 kpc from the center are disk. This criterion brings us down to a sample of 25 MW like galaxies.

### 2.3. Galaxy classification based on the b-value

As already mentioned above, in our analysis, we have used the orbital circularity parameter  $\varepsilon$  to determine the MW-like galaxies with large fraction of stars in the disk. Here we infer the galaxy morphology using a somewhat less used quantity, called the b-value, and compare the final results with the above results, see ([Emami et](#)

**Table 1.** The physical parameters of the TNG50 simulation, including the simulation volume, the box side length, the number of gas and DM particles, the baryon and DM mass and finally the  $z = 0$  Plummer gravitational softening for the DM and stellar components.

Name	Volume [(Mpc) <sup>3</sup> ]	L <sub>box</sub> [Mpc/h]	N <sub>GAS</sub>	N <sub>DM</sub>	m <sub>baryon</sub> [10 <sup>5</sup> M <sub>⊙</sub> ]	m <sub>DM</sub> [10 <sup>5</sup> M <sub>⊙</sub> ]	ε <sub>DM,stars</sub> [kpc/h]
TNG50	51.7 <sup>3</sup>	35	2160 <sup>3</sup>	2160 <sup>3</sup>	0.85	4.5	0.39 → 0.195
TNG50-Dark	51.7 <sup>3</sup>	35	–	2160 <sup>3</sup>	–	5.38	0.39 → 0.195

al. 2020) for more details. Following the approach of Schulze et al. (2020), the b-value is defined as:

$$b = \log_{10} \left( \frac{j_*}{\text{kpc km/s}} \right) - \frac{2}{3} \log_{10} \left( \frac{M_*}{M_\odot} \right). \quad (3)$$

where  $j_*$  refers to the specific angular momentum of stars while  $M_*$  describes the total stellar mass of the galaxy. Based on the above b-value estimate, galaxies can be classified in 3 main categories as disks (with  $b \geq -4.35$ ), intermediates (with  $-4.73 \leq b \leq -4.35$ ) and spheroidal (with  $b < -4.73$ ). Figure 1 presents the b-value vs the halo stellar mass for the full sample of 71 galaxies in the mass range  $(1-1.6) \times 10^{12} M_\odot$  where different galaxy types are marked differently in the figure. Overlaid on the plot, we also show the MW-like galaxies selected from the orbital circularity parameter. Interestingly, all of the inferred as MW-like galaxies are disk, i.e. with  $b \geq -4.35$ , but not every disk galaxy looks like the MW as inferred from  $\varepsilon$  criteria. Below, we keep our previous galaxy classification and limit our current study to MW-like galaxies. In a future work, we aim to compute the shape of disk galaxies in a broader view and compare them with the sample of MW-like galaxies.

#### 2.4. Mass density map

We begin our analysis by presenting the surface number density,  $\Sigma$ , map of stellar halos in a sub-sample of MW like galaxies. Figure 2 presents the projected number density map from a subset of 4 MW like galaxies in our galaxy sample. In different rows, we refer to various galaxies while in different columns we zoom-in further down to the central part of the halo. From the figure, it is evident that stellar halos have very complex profiles and substructures. Owing to this fact, we have to use different algorithms for computing the shape and compare their final outcomes with each other.

### 3. DIFFERENT ALGORITHMS IN THE SHAPE ANALYSIS

Having introduced a sample of 25 MW like galaxies, below we make a comprehensive study about the morphology of the stellar halo as a direct tracer of the galaxy morphology.

We present a couple of different algorithms for computing the shape of the stellar halo. Depending on the

details of the computations, our shape finder algorithms could be divided in two main classes. In both categories, we infer the shape using iterative methods. In the first approach, we compute the shape using a local shell iterative method (LSIM), while in the second method, we analyse the stellar halo shape using an enclosed volume iterative method (EVIM). In Emami et al. (2020), we inferred the DM halo shape using EVIM as the primary method. Here on the other hand, we take LSIM as the main approach. One main reason for this is that star particles are much less abundant than DM particles. This means that the shape is dominated by the few closest shells and the outer layers contribute much less in the final results. Therefore, EVIM is not able to follow the stellar shapes in much detail locally. This however was not a problem for the DM particles and EVIM was very useful method to give us the averaged shape yet with many details of what is going on at every radius and in terms of the rotation of halo.

#### 3.1. Local shell iterative method (LSIM)

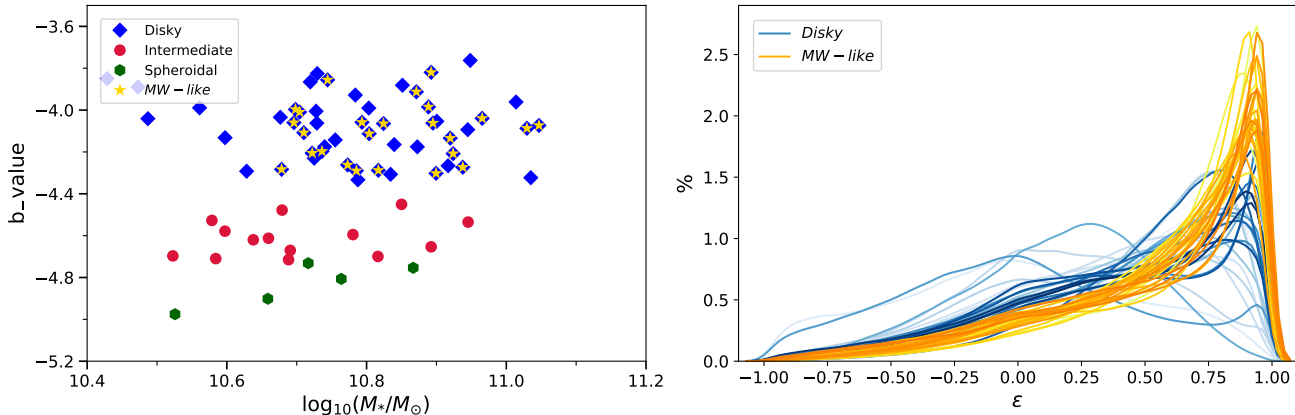
Here we illustrate the LSIM. In this method, we split the range between the radii  $r_{\text{sph}}^i = 2$  kpc and  $r_{\text{sph}}^e = 100$  kpc in  $N = 100$  logarithmic radial thin shells and compute the reduced inertia tensor as:

$$I_{ij} \equiv \left( \frac{1}{M_\star} \right) \times \sum_{n=1}^{N_{\text{part}}} \frac{m_n x_{n,i} x_{n,j}}{R_n^2(r_{\text{sph}})}, \quad i, j = 1, 2, 3. \quad (4)$$

where we have  $M_\star \equiv \sum_{n=1}^{N_{\text{part}}} m_n$  and  $N_{\text{part}}$  describes the total number of star particles inside the thin shell. Furthermore,  $x_{n,i}$  refers to the  $i$ -th coordinate of  $n$ -th particle. Finally,  $R_n(r_{\text{sph}})$  describes the elliptical radius of  $n$ -th particle, defined as:

$$R_n^2(r_{\text{sph}}) \equiv \frac{x_n^2}{a^2(r_{\text{sph}})} + \frac{y_n^2}{b^2(r_{\text{sph}})} + \frac{z_n^2}{c^2(r_{\text{sph}})}, \quad (5)$$

where  $(a, b, c)$  are referring to the axis lengths of the ellipsoid in which hereafter we skip the explicit radius dependence of these functions for brevity. As already mentioned above, in this approach, we compute the shape at some thin shells, where  $0.75 \leq R_n^2 \leq 1$ . At every radius, we iteratively calculate  $I_{ij}$  in the above shells with  $a = b = c = r_{\text{sph}}$  in the first iteration. We then use the



**Figure 1.** (Left) The b-value vs the stellar halo mass for the full sample of galaxies with halo mass in the range  $(1-1.6) \times 10^{12} M_\odot$  in TNG50. Yellow-stars refer to the distribution of the orbital circularity parameter for the MW-like galaxies in our sample. (Right) The distribution of the orbital circularity parameter,  $\epsilon$ , for the disk and MW-like halos in our sample. Different halos are shaded using different colors.

eigenvalues and eigenvectors of the diagonalized inertia tensor to deform the above shell. In addition, in order to control the deformed ellipsoid, we could either take the interior volume or the semi-major axis fixed. This requires different rescaling of the axis lengths as given by  $a = \sqrt{\lambda_1}$ ,  $b = \sqrt{\lambda_2}$  and  $c = \sqrt{\lambda_3}$ . In the former case, the enclosed volume is kept fixed under the following transformations:

$$\begin{aligned} a &= \frac{r_{\text{sph}}}{(abc)^{1/3}} \sqrt{\lambda_1}, \\ b &= \frac{r_{\text{sph}}}{(abc)^{1/3}} \sqrt{\lambda_2}, \\ c &= \frac{r_{\text{sph}}}{(abc)^{1/3}} \sqrt{\lambda_3}. \end{aligned} \quad (6)$$

Here  $\lambda_i$ , ( $i = 1, 2, 3$ ) describes the eigenvalues of the reduced inertia tensor. While in the latter approach, the semi-major is unchanged if:

$$\begin{aligned} a &= \frac{r_{\text{sph}}}{\sqrt{\lambda_{\text{max}}}} \sqrt{\lambda_1}, \\ b &= \frac{r_{\text{sph}}}{\sqrt{\lambda_{\text{max}}}} \sqrt{\lambda_2}, \\ c &= \frac{r_{\text{sph}}}{\sqrt{\lambda_{\text{max}}}} \sqrt{\lambda_3}. \end{aligned} \quad (7)$$

where  $\lambda_{\text{max}} \equiv \text{Max}[\lambda_i, i = (1, 2, 3)]$

In what follows, we adopt the former choice, to get as close as possible to the EVIM. We briefly comment on the latter approach as well. Using the eigenvectors of the inertia tensor as the basis, at every iteration, we rotate all of stars to the frame of principals, as the coordinate frame defined by the three eigenvectors, and we make sure that they present a right handed set of coordinates. In order to get statistically reliable results we require to have at least 1000 stars in a given shell. At all radii, the

halo shape is computed as the ratio of the minor to major axis,  $s = a/c$ , as well as the ratio of the intermediate to the major axis,  $q = b/c$ . We terminate the iteration process once the residual of the shape parameters,  $(s, q)$ , after each iteration gets converged to some level defined by  $\text{Max} \left[ \left( \frac{s - s_{\text{old}}}{s} \right)^2, \left( \frac{q - q_{\text{old}}}{q} \right)^2 \right] \leq 10^{-3}$  with Max referring to the maximum value between the above two quantities. In the following, we only present the points for which the above algorithm has converged.

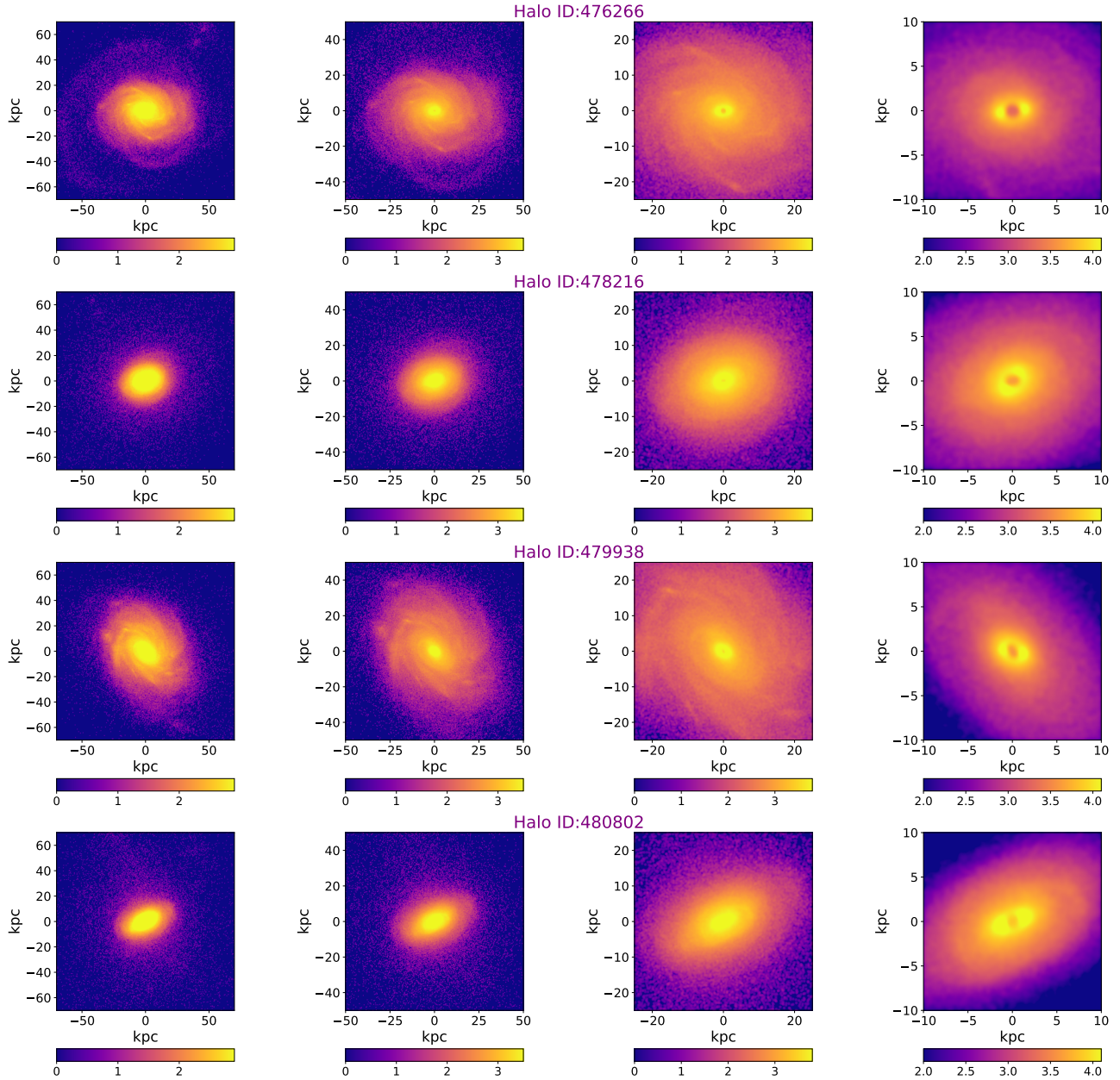
### 3.2. Enclosed volume iterative method (EVIM)

Next, we present the EVIM as a secondary approach in computing the shape of the stellar halo. Generally speaking, this method is very similar to the LSIM with the main difference that at every radius, we replace the thin shell with an enclosed ellipsoid. This may lead to some biases as the number of stars drops significantly from the inner to the outer part of the halo, which naturally leads to an averaged shape, meaning that the physical information may be lost. Indeed, the stellar halo seems to be very simple in most cases with little averaged changes in the radial profile of different angles especially at larger distances. This indicates that the average method for stars does not give us very accurate shape. Owing to this, we skip showing the full details of the results with this approach and instead just present this as a complementary approach.

## 4. SHAPE PROFILE ANALYSIS

Having presented different algorithms for analysing the shape of the stellar halo, below we analyse the halo shape at two different levels; from a statistical and individual perspective.

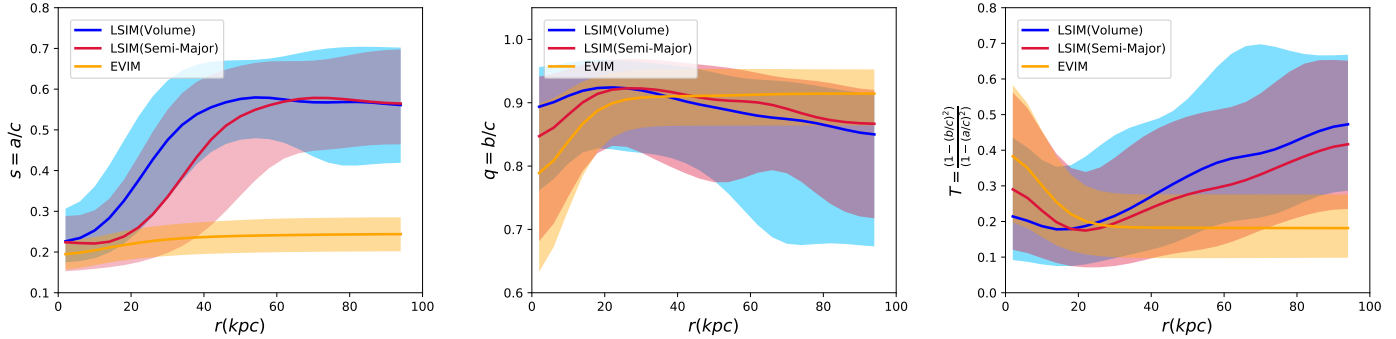
### 4.1. Shape Analysis: ensemble based approach

$\log_{10}(\Sigma/\text{kpc}^2)$  SH Halo

**Figure 2.** Logarithm of the projected number density map (in units of  $\text{kpc}^{-2}$ ) of stellar halo for a sample of 4 MW like galaxies from our galaxy sample in TNG50. Every row presents one galaxy with an ID number. From the left to the right, we zoom-in more on the central part of the halo. We have chosen stars with  $|\varepsilon| \leq 1$ .

Starting from the ensemble approach, in Figure 3, we present the radial profile of the median and 16(84) percentiles for shape parameters ( $s, q, T$ ) in both of the LSIM and EVIM, where  $T \equiv \frac{1-(b/c)^2}{1-(c/a)^2}$  refers to the triaxiality parameter. From the figure, it is evident that both versions of LSIM lead to similar radial profiles for the shape parameters. On the other hand, EVIM gives us a flatter radial curve, especially toward the outskirts of the halo. In addition, while the results of the EVIM

for ( $q, T$ ) are in close proximity to the ones from LSIM, it predicts smaller values for the radial profile of  $s$  parameter compared with the LSIM. This is understood as in the LSIM, less populated outer shells have larger  $s$  parameter, since the halo is getting rounder in the outskirts. On the contrary, the EVIM cannot capture such variation as the inner population of stars somewhat predominant the results in shape estimation. On the other



**Figure 3.** Median and 16(84) percentiles of shape parameters ( $s, q, T$ ) using 3 different algorithms. We studied the shape using two different versions of LSIM and using EVIM. In LSIM(Volume), we compute the shape in local shells with an enclosed volume fixed while in LSIM(Semi-Major), we keep the semi-major axis fixed.

hand, since the  $q$  parameter has a more constant profile, with less variation, both techniques give similar results.

Another interesting aspect of Figure 3 is that the median and percentiles of the triaxiality parameter point to an oblate/triaxial stellar halo. In more detail, the inferred  $T$  profile from both versions of LSIM is oblate in the central part of the halo and becomes triaxial in the outskirts. This is in contrast to the  $T$  profile from the EVIM which is more triaxial in the central part of the halo and gets converted to an oblate shape at the outskirts.

Table 2 presents the median and 16(84) percentiles of the shape parameters ( $s, q, T$ ) for the above three algorithms where the median/percentiles have been computed in the range  $2 \leq r/\text{kpc} \leq 40$ . It is worth pointing out that the median/percentiles depend on the upper cutoff of the radius. We have chosen the above cutoff such that most of the halos have enough converged points in the shape analysis (see the individual halo analysis for more detail). Being mindful of the dependency of the above values on the upper limit of radius, it is interesting that statistically (up to 40 kpc), the  $s$  from the LSIM with fixed semi-major is closer to the EVIM. However, the  $q$  is closer between both versions of LSIM than the EVIM.

The above ensemble based analysis gives us a good sense about the collective behavior of the MW like galaxies in our sample. However, to get a more detailed sense about the morphology of different stellar halos, in the following we turn our attention to the shape analysis at the level of individual halos.

#### 4.2. Shape Analysis: Individual halo approach

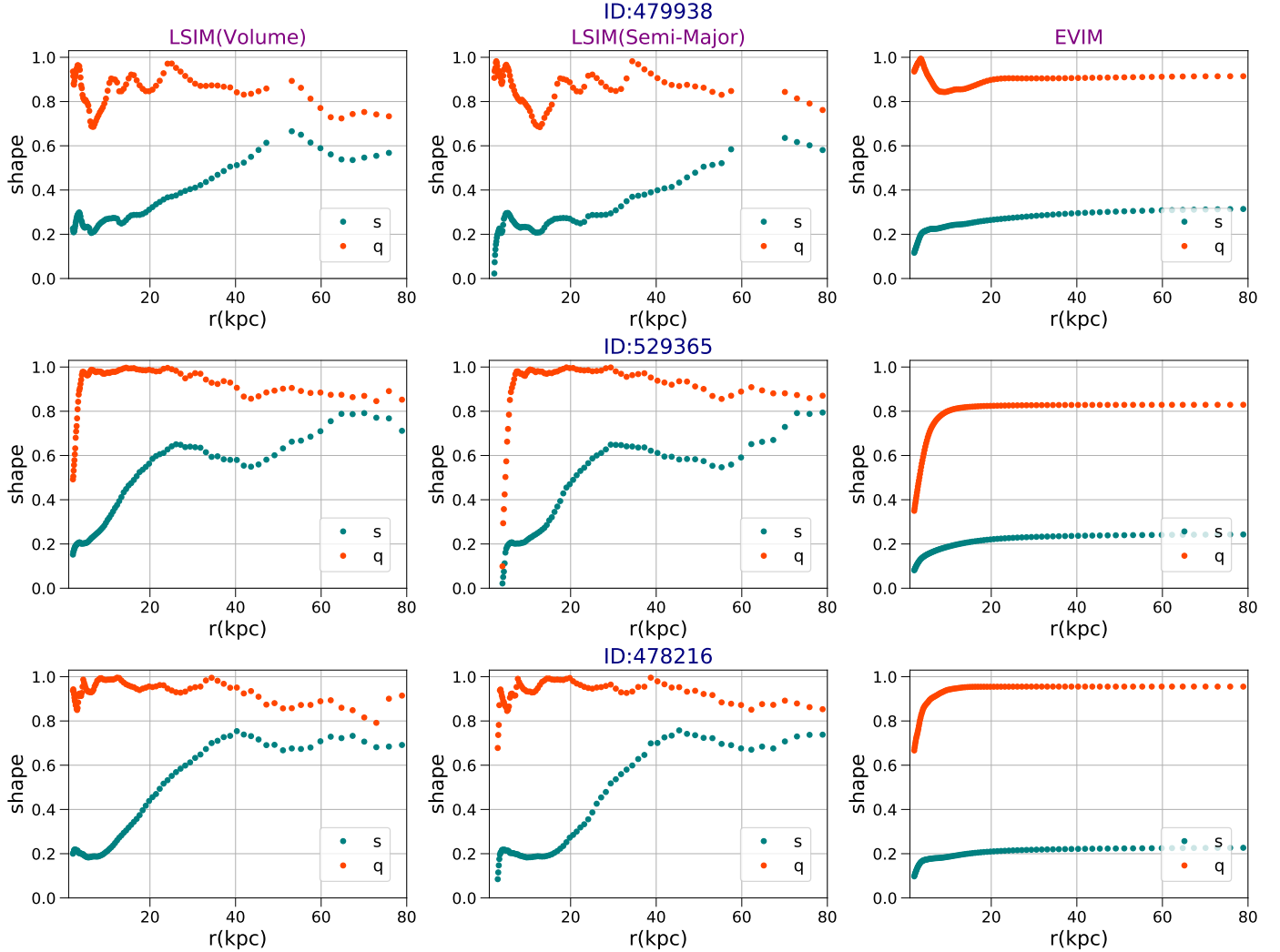
Having presented the stellar halo shape at the statistical level, below we analyse the shape for individual halos. The main goal is to make a classification of different stellar halo types based on the shape of the stellar halo. As already mentioned above, we use LSIM(Volume) as

**Table 2.** Median and 16(84)th percentiles of Stellar halo shape parameters computed from LSIM(Volume), LSIM(Semi-Major) and EVIM. These values are computed in the range  $2 \leq r/\text{kpc} \leq 40$ .

Method	$s$	$q$	$T$
LSIM(Volume)	$0.31^{+0.188}_{-0.103}$	$0.93^{+0.039}_{-0.084}$	$0.19^{+0.215}_{-0.113}$
LSIM(Semi-Major)	$0.24^{+0.109}_{-0.070}$	$0.92^{+0.046}_{-0.102}$	$0.18^{+0.214}_{-0.105}$
EVIM	$0.22^{+0.036}_{-0.038}$	$0.90^{+0.046}_{-0.050}$	$0.19^{+0.092}_{-0.089}$

the main algorithm. However, to make a fair comparison between the above three algorithms, we present the radial profile of the shape parameters for a few halos using all of these methods and compare them in depth. We then make a halo classification using LSIM(Volume).

Figure 4 compares the radial profile of the shape parameters inferred from the above algorithms. From the figure, it is evident that the results of LSIM(Volume) and LSIM(Semi-Major) are very similar. The inferred shape parameters from EVIM, on the contrary, are very smooth and rarely change after the radius of about 20 kpc. This indicates that in EVIM, the shape of outer layers are mostly biased by the interior layers and is a direct consequence of the fact that the stellar density drops sharply towards the outer part of the halos. Owing to this, hereafter we skip presenting the results from EVIM. In addition, as the results from different versions of LSIM are fairly close, we just present the results from LSIM(Volume) as the main method. Having compared the outcome of different shape finder algorithms, below we focus on the stellar halo shape from individual ha-



**Figure 4.** Comparison between the radial profile of the shape parameters using three different algorithm LSIM(Volume), LSIM(Semi-Major) and EVIM.

los and use this to classify stellar halos in our galaxy sample.

Following the approach from Emami et al. (2020), we put stellar halos in two main classes, (i) Twisted, and (ii) Twisted-Stretched halos, in which halos associated with different categories behave differently in terms of their axis lengths as well as the radial profile of the halo orientation specified in terms of their local eigenvectors.

Below we describe each of these classes in some depth and we present one example from each class. More detail about the entire halo sample are found in appendix A.

#### 4.2.1. Twisted halos

Halos belonging to this category show some level of gradual rotations in their radial profiles. To quantify the twists, we shall compute the angles between the sorted eigenvectors, (min, inter, max), with different fixed vectors in the 3D such as  $L_{\text{tot}}^{\parallel}$ , which refers to the total an-

gular momentum of stars, and three basis of the Cartesian coordinate system in the TNG box, i.e.  $\hat{i}, \hat{j}$  and  $\hat{k}$ . The amount of the total rotation differs from one halo to another. There are 13 halos in this category. The radial profile of such halos are described in appendix A.

#### 4.2.2. Twisted-Stretched halos

As the second class, here we describe the Twisted-Stretched halos. In brief, such halos may demonstrate both a gradual (owing to the halo twist) as well as abrupt rotations (because of the halo stretching) in their radial profiles. Halos in this class may also be cases for which it is rather hard to distinguish whether the large rotation is owing to the twist or stretching or both simultaneously. Here stretching occurs when the ordering between different eigenvalues changes at some radii. Consequently, the angles of the corresponding eigenvectors with different fixed vectors is expected to change

by 90 deg owing to the orthogonality of different eigenvectors. However, since the halo itself is also rotating, in some halos, these two rotations get mixed and it is difficult to fully distinguish them. For example, halo 23, with the ID number 530330, is one such halo. In this halo, around the crossing radii, at the radius of 10 kpc, the angles of the associated eigenvectors to the intermediate and maximum eigenvalues do not change by 90 deg. It well might be that the halo is also rotating in the opposite direction and thus the net rotation is less than 90 deg but it is hard to confirm this. Owing to this, we classify halo 23 as twisted-stretched. There are in total 12 halos in this class.

Having introduced different classes of halos, in Figure 5, we present one example for each of the above classes. The first example refers to a twisted halo in which the halo experiences a gradual rotation from the inner to the outer part of the halo. The second example, on the other hand, describes a twisted-stretched halo with more abrupt change of axis.

#### 4.3. Impact of threshold on SH definition on the shape analysis

So far we computed the stellar halo shape using all of stars out to 100 kpc. Here we generalize the above consideration and study the impact of the threshold in defining the stellar halo in the shape analysis. This is motivated as former studies sometimes define the stellar halo based on the orbital circularity parameter. Monachesi et al. (2019) defined the stellar halo based on stars with  $\varepsilon \leq 0.7$ . Here we explore the impact of changing the cutoff in the SH definition and place our criterion based on orbital circularity parameter of individual stars to be below  $\varepsilon \leq [0.6, 0.7, 0.8, 1.0]$  in choosing the stars as the part of the SH. More explicitly, each time we mask out all stars that have  $\varepsilon$  above the aforementioned thresholds and compute the shape accordingly.

Figure 6 presents the radial profile of the median and 16(84) percentiles of shape parameters, ( $s, q, T$ ), for the above thresholds.

Quite interestingly, increasing the upper limit in  $\varepsilon$  decreases the profile of median(percentiles) of  $s$  at smaller radii, where disk stars are mostly located. This is to be expected, as increasing the threshold of  $\varepsilon$ , we add more rotationally supported stars which are part of the stellar disk. Subsequently, the shape becomes progressively more oblate. On the other hand, this does not significantly affect the radial profile of median(percentiles) of  $q$ . Consequently, the radial profile of percentiles of  $T$  only slightly shifts down.

Table 3 summarizes the median and percentiles of the shape parameters for the above thresholds. In our anal-

ysis, we limit the radial range to  $2 \leq r/\text{kpc} \leq 40$ . From the table it is inferred that increasing the threshold in the SH definition (i) decreases the median of all of the shape parameters. (ii) However the amount of suppression in  $s$  is larger than the changes in  $q$ . This is understood as increasing the threshold in  $\varepsilon$  makes the halo more oblate and thus further decreases the median of the  $s$ .

**Table 3.** Median and 16(84)th percentiles of Stellar halo shape parameters as a function of the threshold in defining the stellar halo. These values are computed in the range  $2 \leq r/\text{kpc} \leq 40$ .

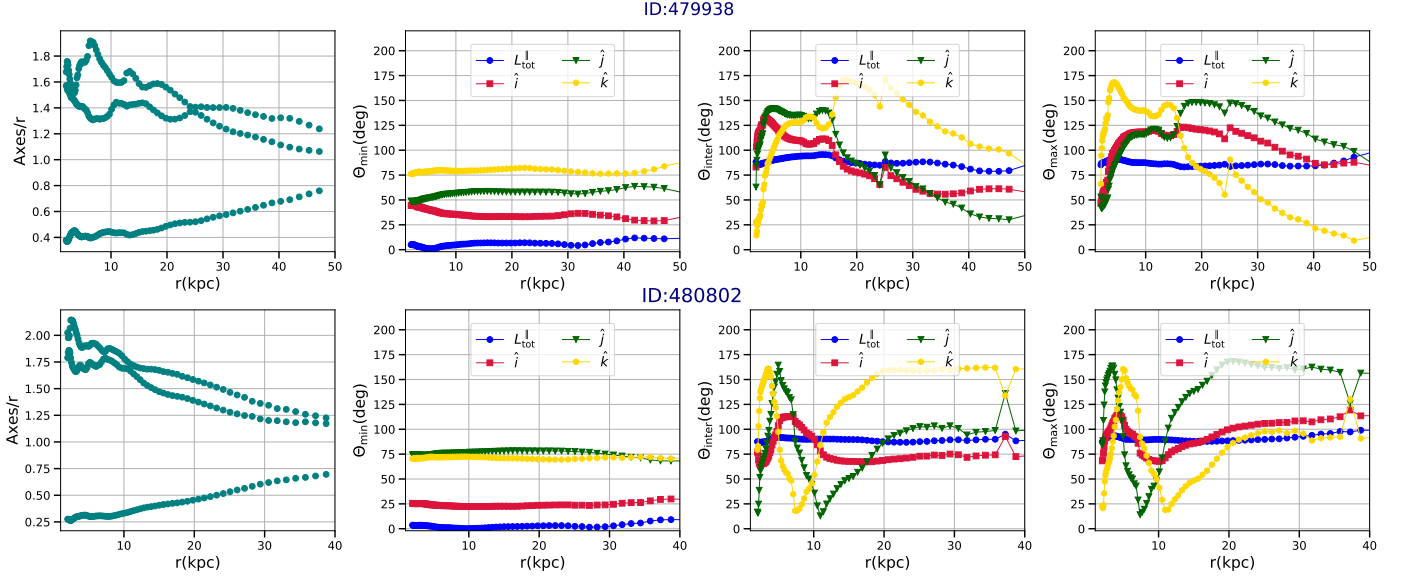
Threshold	$s$	$q$	$T$
$\varepsilon \leq 0.6$	$0.641^{+0.118}_{-0.132}$	$0.942^{+0.034}_{-0.059}$	$0.204^{+0.181}_{-0.115}$
$\varepsilon \leq 0.7$	$0.595^{+0.126}_{-0.146}$	$0.941^{+0.033}_{-0.074}$	$0.195^{+0.173}_{-0.112}$
$\varepsilon \leq 0.8$	$0.537^{+0.121}_{-0.153}$	$0.934^{+0.037}_{-0.122}$	$0.191^{+0.206}_{-0.110}$
$\varepsilon \leq 1.0$	$0.308^{+0.188}_{-0.103}$	$0.926^{+0.039}_{-0.084}$	$0.189^{+0.215}_{-0.113}$

#### 4.4. Different visualizations of the stellar halo

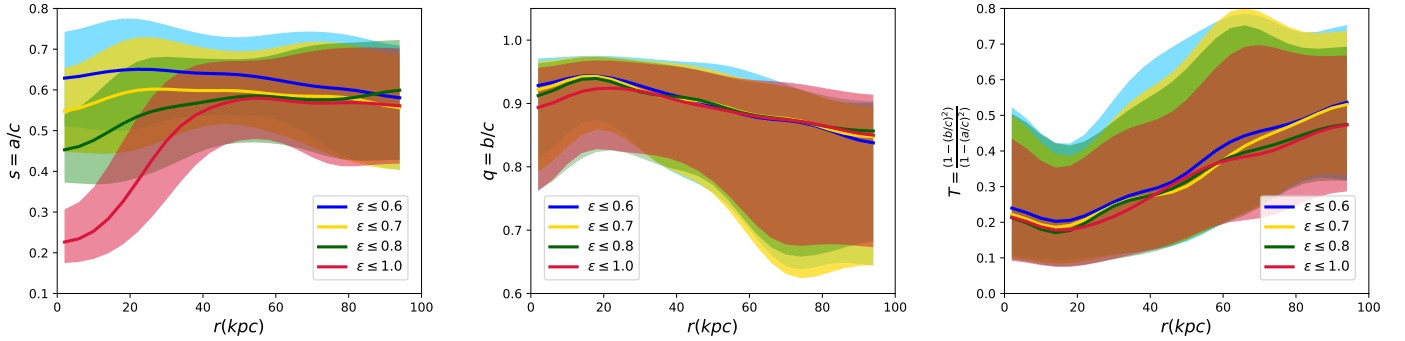
Having presented the shape profile for individual halos, here we make different visualizations for typical halos in the above two classes of stellar halos.

In Figures 7-8, we present the 2D projected surface density for one example of the twisted and twisted-stretched halos, respectively. In each figure, we present the surface density at few different radii. In each radius, we use the results of the shape analysis, after the convergence, and make an image using the stars corresponding to this radius. From the figures, it is evident that the halo is rotating, in Figure 7, while it is stretching, in Figure 8.

Moving to 3D, in Figures 9-10, we present the trajectory of the 3D eigenvectors of inertia tensor for the same twisted and twisted-stretched halos as above. Evidently, while the twisted halo shows a rather gradual rotation in a wider range of locations, the twisted-stretched halo experiences a more abrupt change of angles in its radial profiles. That is to say that maybe the most visible difference between these halos comes back to the abruptness of the transition of angle. Finally, it is crucial to note that if the axis ratio of the axes that are



**Figure 5.** The radial profile of the Axes/ $r$  as well as the angle of min-inter-max eigenvectors with few fixed vectors in space. (upper) an example of twisted halo. (Bottom-panel) an example of twisted-stretched halo.



**Figure 6.** Impact of changing the threshold of the stellar halo,  $\epsilon$ , on the radial profile of the median and 16(84) percentiles of shape parameters.

re-orienting is not close to unity, then we're certainly not dealing with a stretching but a twisting.

## 5. COMPARISON BETWEEN THE SHAPE OF THE DM AND THE STELLAR HALOS

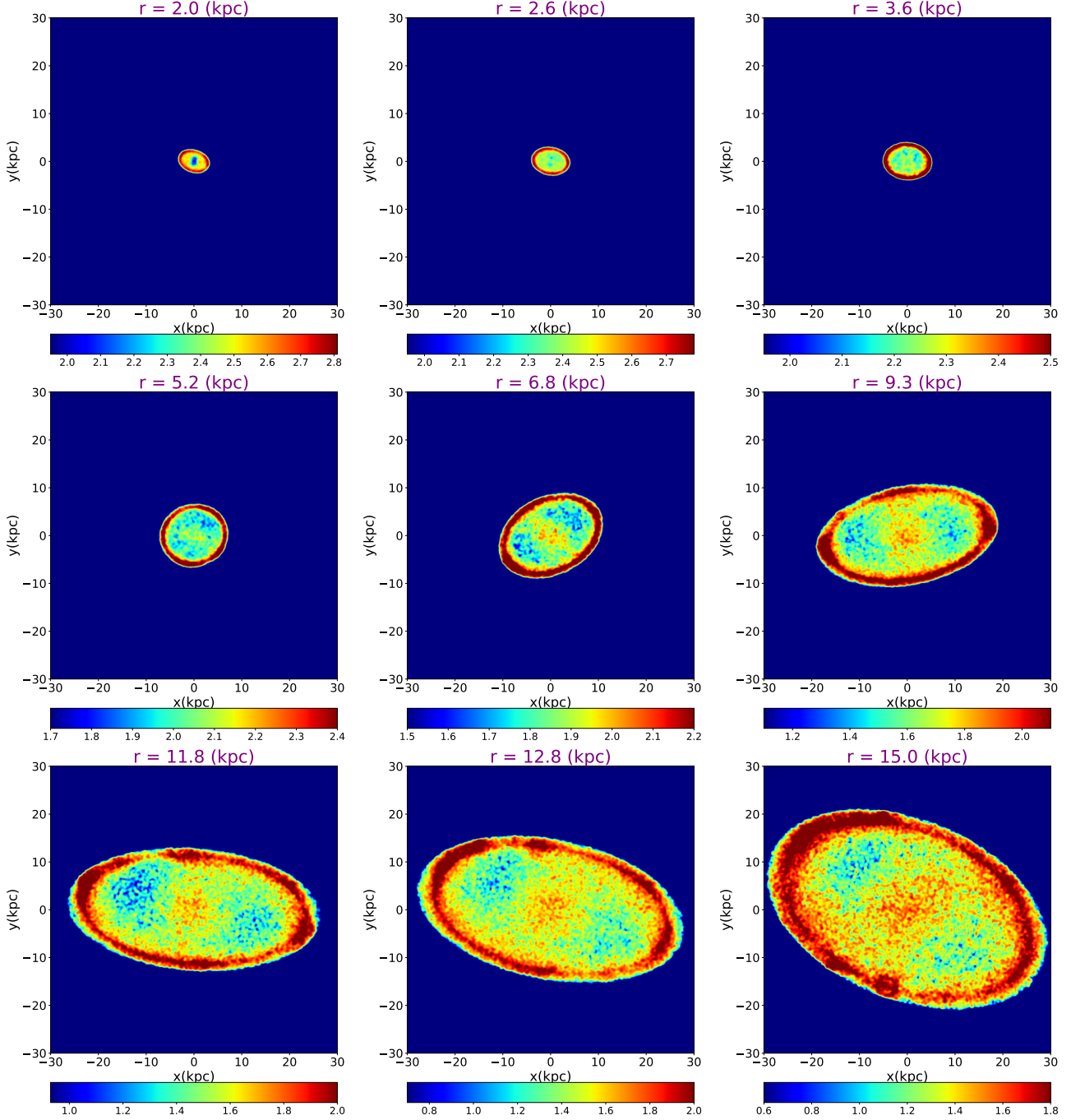
Having computed the shape of the stellar halos in detail, here we make some comparisons between the eigenvectors of the inertia tensor associated with the DM halo, inferred from Emami et al. (2020), and the results of this work for the stellar halo. Since in Emami et al. (2020) we used the EVIM as the main algorithm, while here we mainly use the LSIM, we do the comparison separately using both of these methods. As we point out in what follows, this enables us to look at the correlations both in the enclosed sense, from the EVIM, as well as locally, LSIM. Our expectation is that the EVIM method gives us smoother profiles while the LSIM provides more

radially varying correlations. To make the comparison we take the following steps:

- (i) Make the same radial bins for both DM and stellar halo (SH) and compute the shape for each using both of EVIM and LSIM separately.
- (ii) Mask over the radii and only look at the radii in which both of these algorithms have converged.
- (iii) Compute the angles between  $V_{DM}$  and  $V_{SH}$ , which refer to the eigenvectors of the DM and SH, respectively. Since we have 3 sets of orthogonal vectors, we end up having 9 different angles. Sorting the eigenvectors in terms of min, inter and max eigenvalues, we get the following array of angles at every location:

$$\Theta = \left[ \theta_{mi-mi}, \theta_{mi-in}, \theta_{mi-ma}, \theta_{in-mi}, \theta_{in-in}, \theta_{in-ma}, \theta_{ma-mi}, \theta_{ma-in}, \theta_{ma-ma} \right]. \quad (8)$$

## Twisted, ID:501725



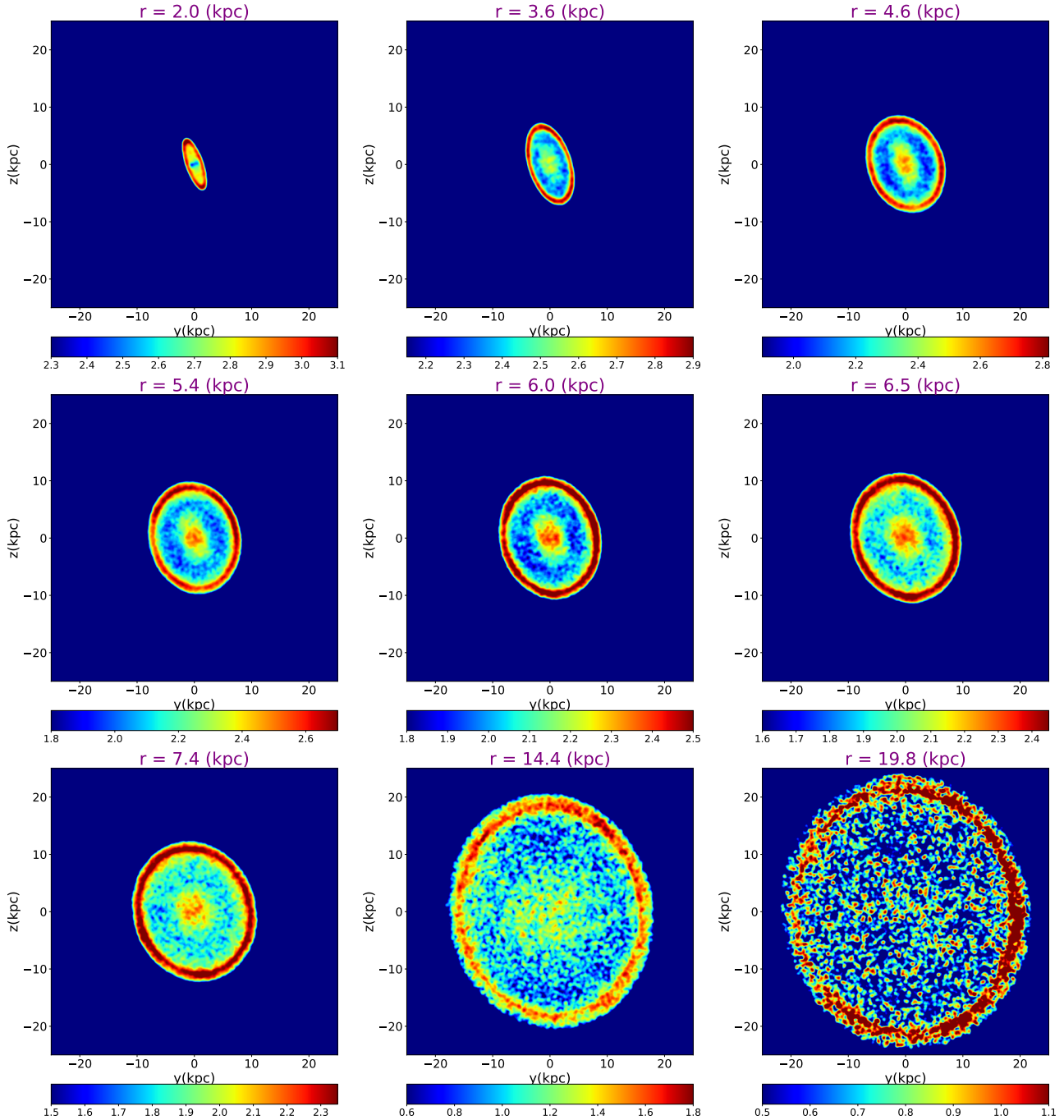
**Figure 7.** 2D projection of the surface density of the mass in 3D thin shells (in units of  $10^5 \times M_{\odot} \text{ kpc}^{-2}$  for a twisted SH. Evidently the halo is re-orienting at different radii. We have computed the projection along a fixed direction in space,  $z$  direction in the TNG coordinate.

where we have used (mi, in, ma) in replace to (min, inter, max) for the sake of brevity. In addition, the first index refers to DM while the second one describes the stellar halo.

As we have sorted the eigenvectors according to their corresponding eigenvalues, a good test for the similarity

of the DM and stellar halo would be to check the magnitude of mi-mi, in-in and ma-ma angles. The smaller these values are, more similar the orientation of the DM halo and SH halo would be. Owing to this, in what follows, we make a special emphasis on the magnitude of these angles. In figures 11 and 12, we present all 9 of the

## Twisted-Stretched, ID:506720

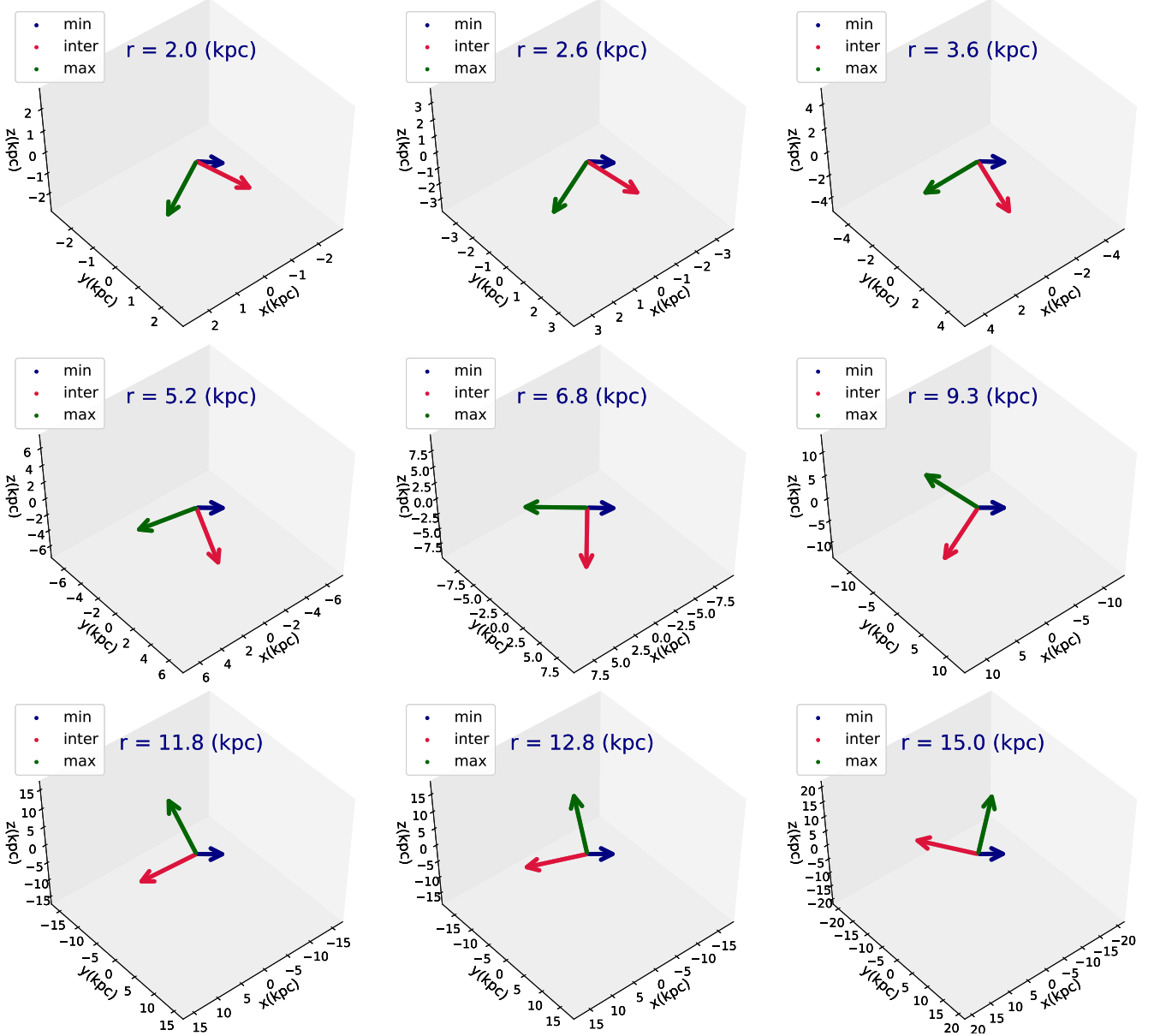


**Figure 8.** 2D projection of the surface density (in units of  $10^5 \times M_{\odot} \text{ kpc}^{-2}$  for a twisted-stretched SH. Starting from an oblate shape in 3D initially, the halo is stretching and becoming more spherical at larger radii. We have computed the projection along the  $x$  direction in the TNG coordinate.

above angles from the EVIM and LSIM, respectively. To make the above 3 angles more manifest, we have plotted them with slightly thicker lines and with the following color sets; mi-mi (dashed, red), in-in (orange), ma-ma (dashed, blue). Below we describe few common features of these comparisons.

(1) First and foremost, comparing Figure 11 with Figure 12, it is evident that while the mi-mi angle is fairly small and stable, the radial profile of in-in and ma-ma are a lot more fluctuating in LSIM than in EVIM. That makes sense as in LSIM the intermediate and maximum eigenvalues are swinging a lot and sometimes it

## Twisted, ID:501725



**Figure 9.** Three dimensional orientation of the reduced inertia tensor for a twisted halo. There is a smooth rotation in the orientation of different eigenvectors radially.

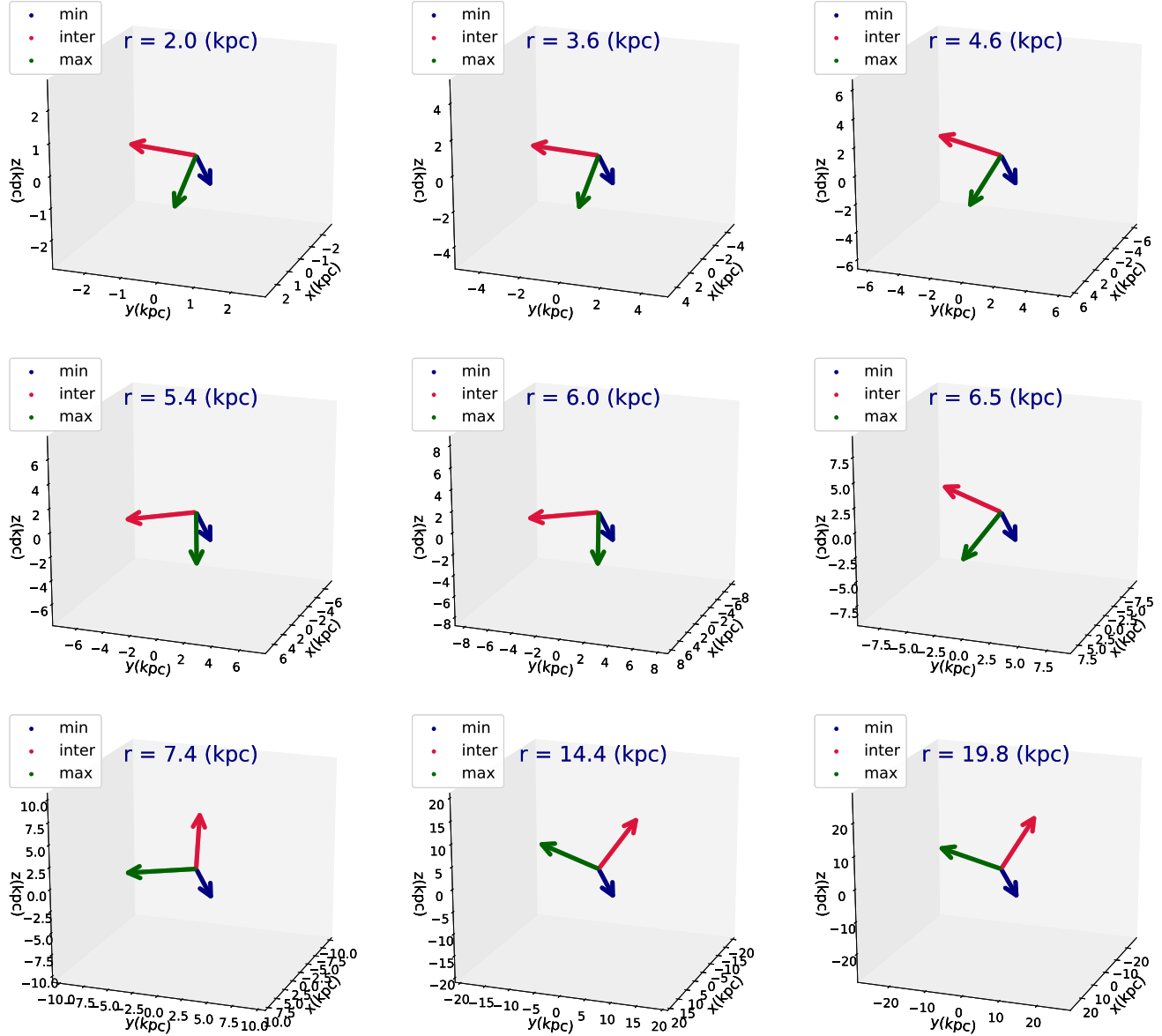
is very hard to distinguish them from each other. However, since their corresponding eigenvectors are orthogonal to each other, wherever these lines swing around each other, the angle profile gets dominated by noise. So care must be taken when we compare these profiles with LSIM.

(2) The fact that mi-mi is fairly small in both of these methods is very intriguing demonstrating that the symmetric axes of DM and SH are fairly matched. This is because the min eigenvectors in both halos are pointing toward the total angular momentum of the system. This observation confirms that in most cases, the symmetry

axis of DM and SH are almost aligned with each other. At smaller radii this seems to be very natural and might be due to the interaction of the DM halo with the stellar disk. Owing to this interaction the DM halo is getting aligned with the total angular momentum of the stars. In some cases such alignment remains the same at larger radii. Others show some levels of misalignment farther out from the center, though.

(3) From Figure 11, it is evident that in most cases, the radial profile of in-in and ma-ma are fairly small close to the center. However, in more than half of halos, the angle starts enhancing farther out from the center

## Twisted-Stretched, ID:506720



**Figure 10.** Three dimensional orientation of the reduced inertia tensor for a twisted-stretched halo. There is a quick rotation in the orientation of different eigenvectors radially.

and gets to its maximum value at larger radii. This means that beyond the typical size of the disk, about 10 kpc, DM and SH profiles are getting misaligned in the plane perpendicular to the total angular momentum. Although very oscillatory, the same conclusion may be drawn for Figure 12 as well. The main reason for this is that, anytime that the inter and max eigenvalues cross each other, the curve of in-in and ma-ma gets enhanced and the other two angles in-ma and ma-in decrease. This indicates that it could be very challenging to identify the inter and max eigenvectors that are matched from DM to SH when the swing occurs. Being mindful of

this technical difficulty, it is fair to say that by a broad majority, the radial profile of the eigenvectors of DM and SH in the stellar disk plane are rather close. They may get however misaligned beyond the disk scale.

(4) In summary, it seems that the profile of the DM and SH are fairly similar within the stellar disk. In the plane of the disk, their eigenvectors get misaligned while they remain mostly aligned perpendicular to the stellar disk.

Finally, to get a 3D intuition regarding to the similarity of the DM and SH profiles, in Figure 13, we present the 3D trajectory of the eigenvectors of a twisted halo

at few different locations. Solid lines describe the DM profile, while the dashed lines refer to the SH. It is evidently seen that both of EVIM and LSIM predict similar profiles for the eigenvectors of the DM and SH. Consequently, the min, inter and max eigenvectors from these two approaches are fairly close. This is however not hold entirely and at the last radii, the halo experiences another rotation in which the inter and max eigenvectors become perpendicular to each other.

## 6. CONNECTION TO SUBSTRUCTURE

So far we only investigated the impact of central halos in our analysis. Below we generalize our consideration and analyze the impact of different substructures, by using FoF group catalogue, in galaxy morphologies. We particularly study the impact of substructures on the orbital circularity parameter and the shape of SH.

### 6.1. Impact of FoF substructures on $\varepsilon$

Here we study the impact of substructures in the orbital circularity parameter,  $\varepsilon$ . As it turns out, the position of substructures are essential in determining the radial distribution of  $\varepsilon$ . Stellar particles located very far away from the galactic center may have a dominant impact on the total angular momentum of the stellar halo while having no effects on the angular momentum of the disk. Subsequently, depending on their orbital motions, in some cases they may counter-rotate with respect to the disk particles, located at  $r \leq 10$  kpc, and thus shift the radial distribution of  $\varepsilon$  slightly or even convert it from disk- to a bulge-like galaxy. Below we present some examples in which including substructures may shift the radial distribution of  $\varepsilon$ . Since, by selection, the central halo in all of these examples remains MW like, i.e. demonstrates a well-defined disk, to avoid any confusions about the morphology of galaxy group, we put a mask over the distance of particles and disregard stellar particles beyond 150 kpc in computing the total angular momentum and thus in  $\varepsilon$ . As we show, such a mask removes counter-rotating particles and the final  $\varepsilon$  distribution remains disk-like, i.e. peaks near unity.

Figure 14 presents the radial distribution of  $\varepsilon$  for a subset of 5 galaxies representative of our galaxy samples. In every example, the left panel presents the distribution for central particles without any substructures. The middle column shows  $\varepsilon$  in the presence of all of substructures and with no radial truncation. The right panel presents  $\varepsilon$  with substructures that are truncated above  $r = 150$  kpc. From the figure, it manifests that substructures with no radial mask may easily shift the orbital circularity parameter to the left and convert it from disk- to a bulge-like galaxy.

### 6.2. Impact of FoF substructures on the shape

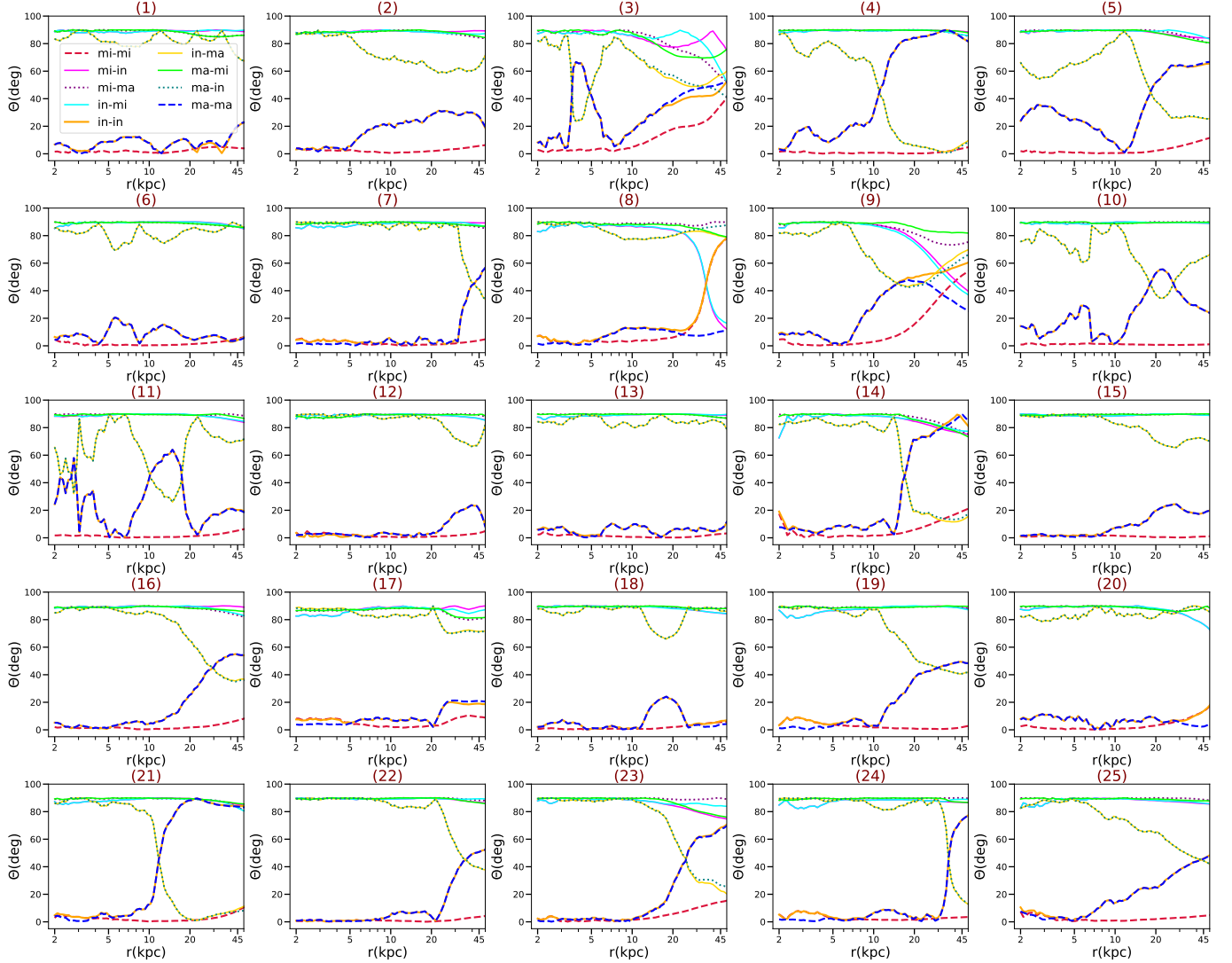
In this section, we investigate the impact of FoF substructures on the shape of the stellar halo, for which we take into account all of the stellar substructures while computing the shape. Figure 15 presents the radial profile of the shape parameters ( $s, q, T$ ) for the central subhalo and the FoF group halo. It is evidently seen that the profile of the median and percentiles are fairly close to each other. Furthermore, to get an intuition on how individual halos look like, in Figure 16, we draw the Axes/ $r$  ratio for two typical halos in the entire sample. Here the left columns refer to the central halo while the right column shows the Axes/ $r$  for the FoF group stars. While the profile of the halo from the first row shows slightly different behavior, the one from the second row is completely similar from the central to FoF group halo. The same applies to the rest of halos (not shown) where in some of them there are some small changes in the inner part of the halo or at the outskirts of the halo.

## 7. CONNECTION TO OBSERVATIONS FROM THE LITERATURE

Having computed the shape of SH theoretically, below we compare them with the observational data from the previous literature. As discussed in Bland-Hawthorn & Gerhard (2016) and references therein, measuring the first-order shape and structure of the halo is extremely challenging in its own right, let alone additional higher-order effects such as twisting or stretching. As a result, here we instead focus on the shape parameters ( $s, q$ ) and leave a detailed analysis of twisting and stretching to a future work.

In our analysis, we extensively use the observational constraints on the shape of stellar and DM halos as provided in Bland-Hawthorn & Gerhard (2016).

From the observations, we may measure the stellar density profile of MW halo. There have been several studies trying to estimate the stellar density as a function of radius (Vivas & Zinn 2006; Ivezić et al. 2008; Belokurov et al. 2014). Subtracting populations of stars which belong to large substructures (see e.g. Bell et al. 2008; Belokurov et al. 2014) we end up with a smooth stellar halo component (although more recent work such as Naidu et al. (2020) has brought even this into question). The inferred density profile can be fitted to various profiles, including a single power-law (SPL), a broken power-law (BPL), or an Einasto Profile. These can also take axisymmetric,  $r^2 = (x^2 + y^2 + z^2/q^2)$ , or triaxial,  $r^2 = (x^2 + y^2/q^2 + z^2/s^2)$ , shapes with shape parameters  $s, q$  analogue to our shape parameters. Note that since our results point us to a very mild triaxial

$\arccos(V_{DM} \cdot V_{SH}):(\text{EVIM})$ 


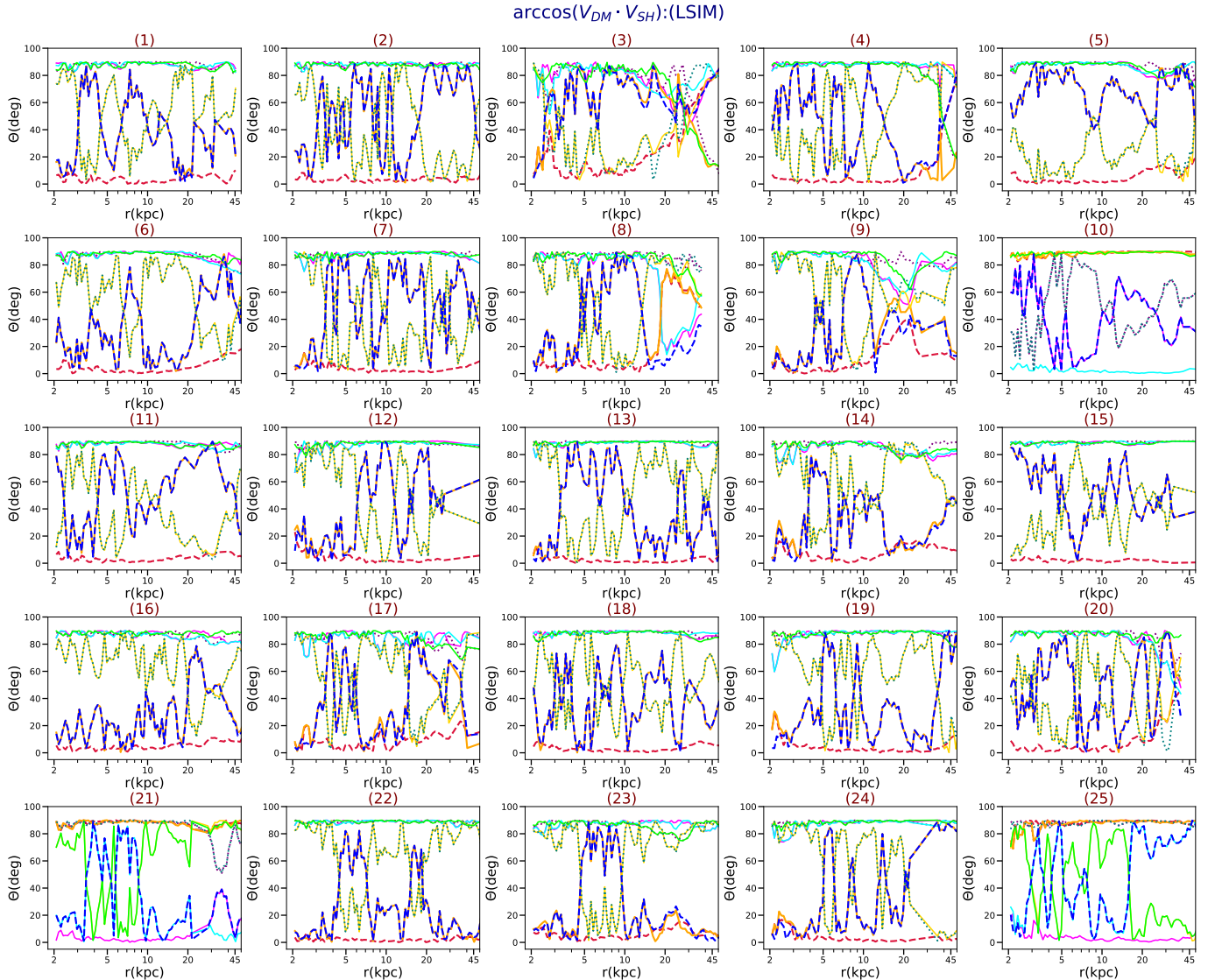
**Figure 11.** Comparison between the radial profile of the angles of different eigenvectors of DM and SH using the EVIM. The eigenvectors are ordered as (min, inter, max), which are shown as (mi, in, ma) for brevity. There are in total 9 different angles. The DM and SH halos are more similar if the min-min, inter-inter and max-max angles are minimal and the rest of them are maximal.

shape, we expect that comparisons to axisymmetric fits should still remain reasonable.

Using a maximum likelihood approach, Deason et al. (2011) modeled the density profile of blue horizontal branch (BHB) and blue straggler (BS) stars and applied it to photometric catalogue of Sloan Digital Sky Survey (SDSS) data release 8 (DR8). As they showed, it provides a robust measurement for the shape of MW stellar halo. As a part of their analysis, they provided the fit to a SPL profile with a triaxial shape and constant shape parameters. Rewriting this in terms of our shape parameters, we get  $s = 0.5^{+0.02}_{-0.01}$  and  $q = 0.71^{+0.03}_{-0.03}$  covering a radial range (4-40) kpc. Since this measurement is extended up to 40 kpc, to closely compare our

results with that of SDSS, we shall repeat the computation for the median and 16(84) percentiles of  $(s, q)$  up to this radius. In addition, to fully account for the impact of changing the threshold of  $\varepsilon$  in the stellar halo, we compute the median(percentiles) of the shape for few thresholds of  $\varepsilon$ .

Bell et al. (2008) used a sample of main sequence turnoff (MSTO) stars from Sloan Digital Sky Survey (SDSS) DR5 and explored the overall structure of the stellar halo in MW. They fitted an oblate and triaxial BPL to data and found a best fit for  $0.5 \leq s \leq 0.8$  with a mild triaxial parameter  $q \geq 0.8$ . Their best fit for  $s$  from axisymmetric and triaxial was very similar indi-



**Figure 12.** Comparison between the radial profile of the angles of different eigenvectors of DM and SH using the LSIM. See the caption of Figure 11 for more details.

indicating that the results of mild triaxial fit is not very far from the axisymmetric results.

Sesar et al. (2013) used RR Lyrae stars (RRLS) chosen from a recalibrated LINEAR data set and fitted an axisymmetric density profile to data. They found a slightly larger flattening parameter  $s = 0.63 \pm 0.05$  than Deason et al. (2011). This result is compatible with the results of other observational teams using RRLS (Watkins et al. 2009; Sesar et al. 2010; Faccioli et al. 2014)

Figure 17 summarizes the above constraints on the shape parameters of the stellar halo. From the figure, it is inferred that observations of Sesar et al. (2013) and Bell et al. (2008) are more compatible with a smaller  $\varepsilon$  threshold. On the contrary, Deason et al. (2011) seem to prefer slightly larger threshold in  $\varepsilon$ , though their inferred  $q$  parameter is rather low. This comparison makes it

clear that the observational results may depend strongly on the type of the stellar tracer as well as the approach.

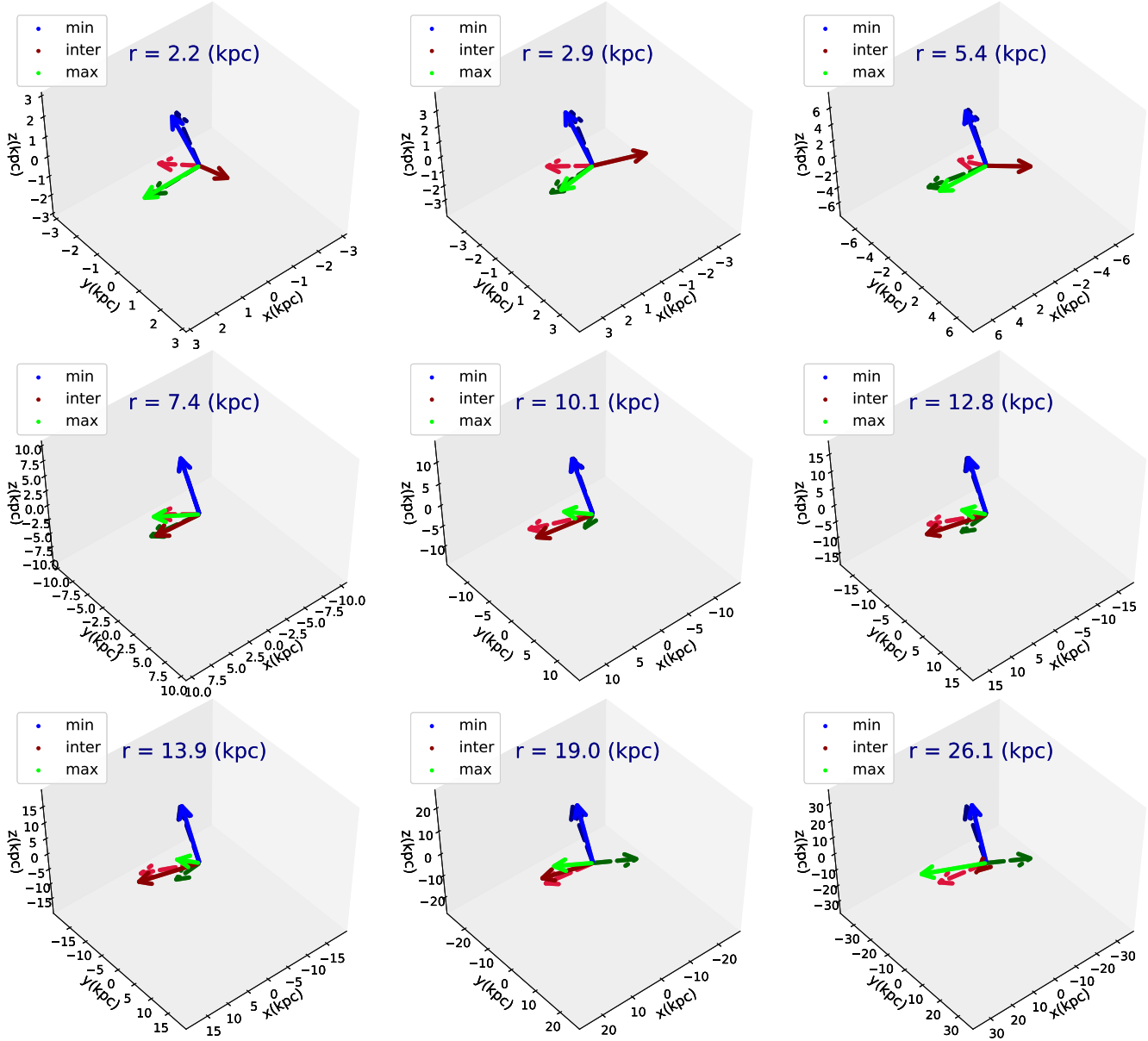
## 8. SUMMARY AND CONCLUSION

In this paper, we studied the morphology of stellar halos in a sample of 25 MW like galaxies in TNG50 of the IllustrisTNG project. We explored the stellar halo shape using two different algorithms. In the first approach, we computed the shape using an enclosed volume iterative method (EVIM) and in the second (main) approach, we analysed the shape using a local in shell iterative method (LSIM).

Below we summarize the main points of the paper,

- We explicitly showed that while EVIM leads to a smooth shape profile, LSIM gives us more information about the substructures. Owing to this and as the re-

Twisted DM(-), SH(--), ID:476266



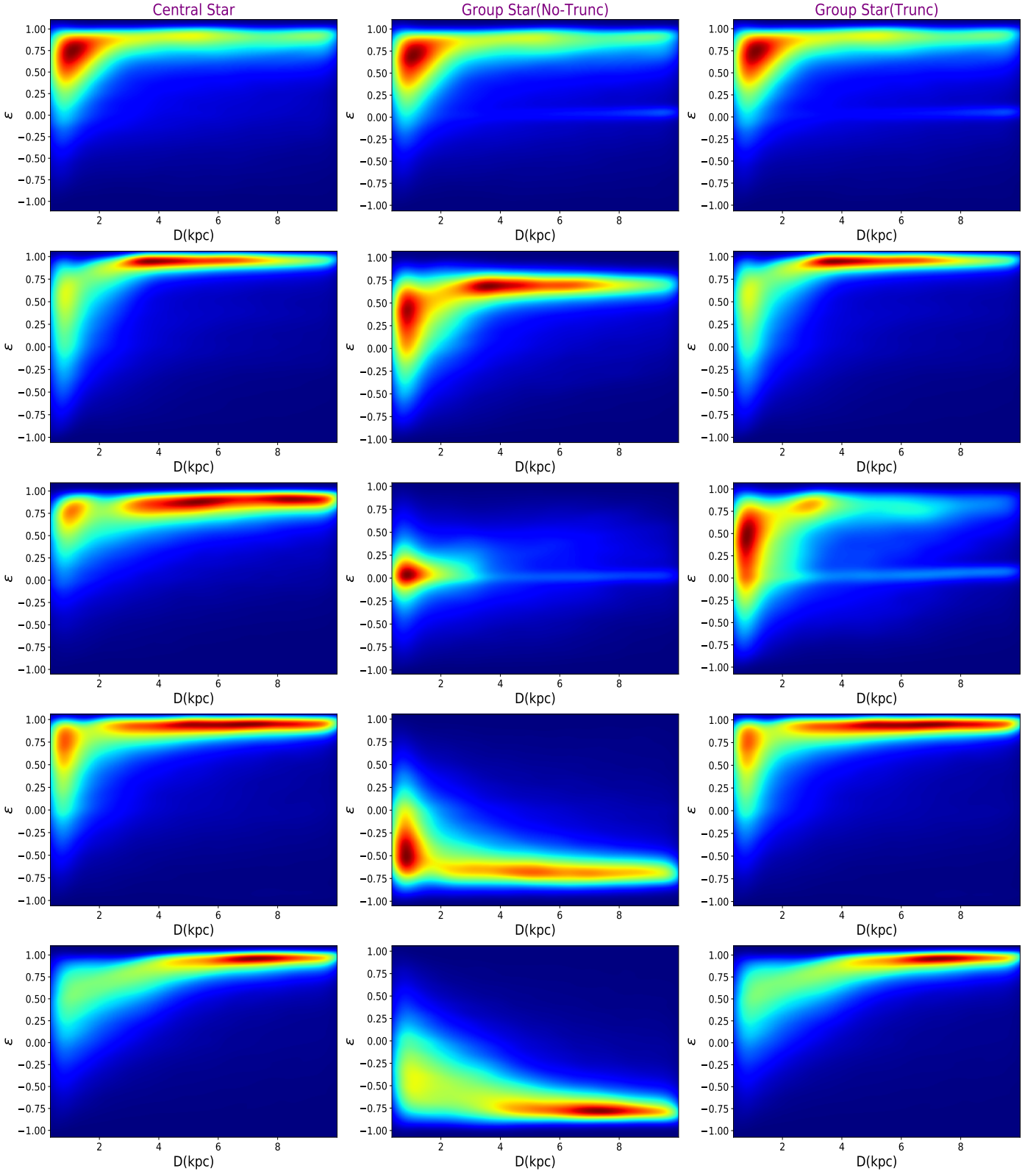
**Figure 13.** Three dimensional orientation of the reduced inertia tensor from the DM and SH for one example of twisted halo.

cent observations [Naidu et al. \(2020\)](#) have shown that the MW is truly made of many substructures, the local based approach is more favored here and we have thus used LSIM as the main approach in this work.

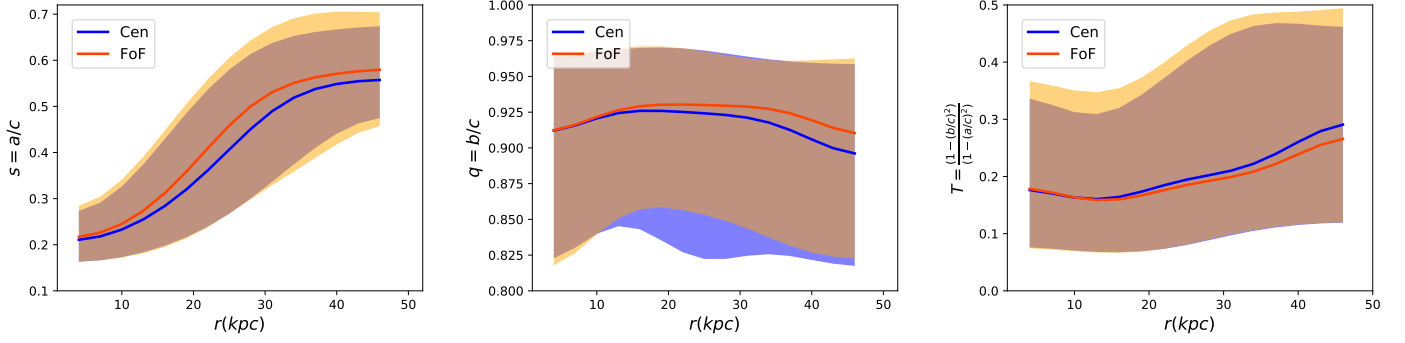
- We inferred the shape both at the statistical level as well as for individual level and classified the halos in two different categories. Twisted halos present a gradual rotation throughout the halo. There are in total 13 halos in this category. Twisted-Stretched halos, on the other hand, present more abrupt radial rotation. There are 12 halos in this class. We visualized the halos in both of the above samples and showed that the halo is rotating/stretching, respectively.

- We studied the impact of the threshold on the orbital circularity parameter,  $\varepsilon$ , in defining the stellar halo in the final inferred shape and explicitly showed that adding more stars, from the disk, make the halo more oblate.

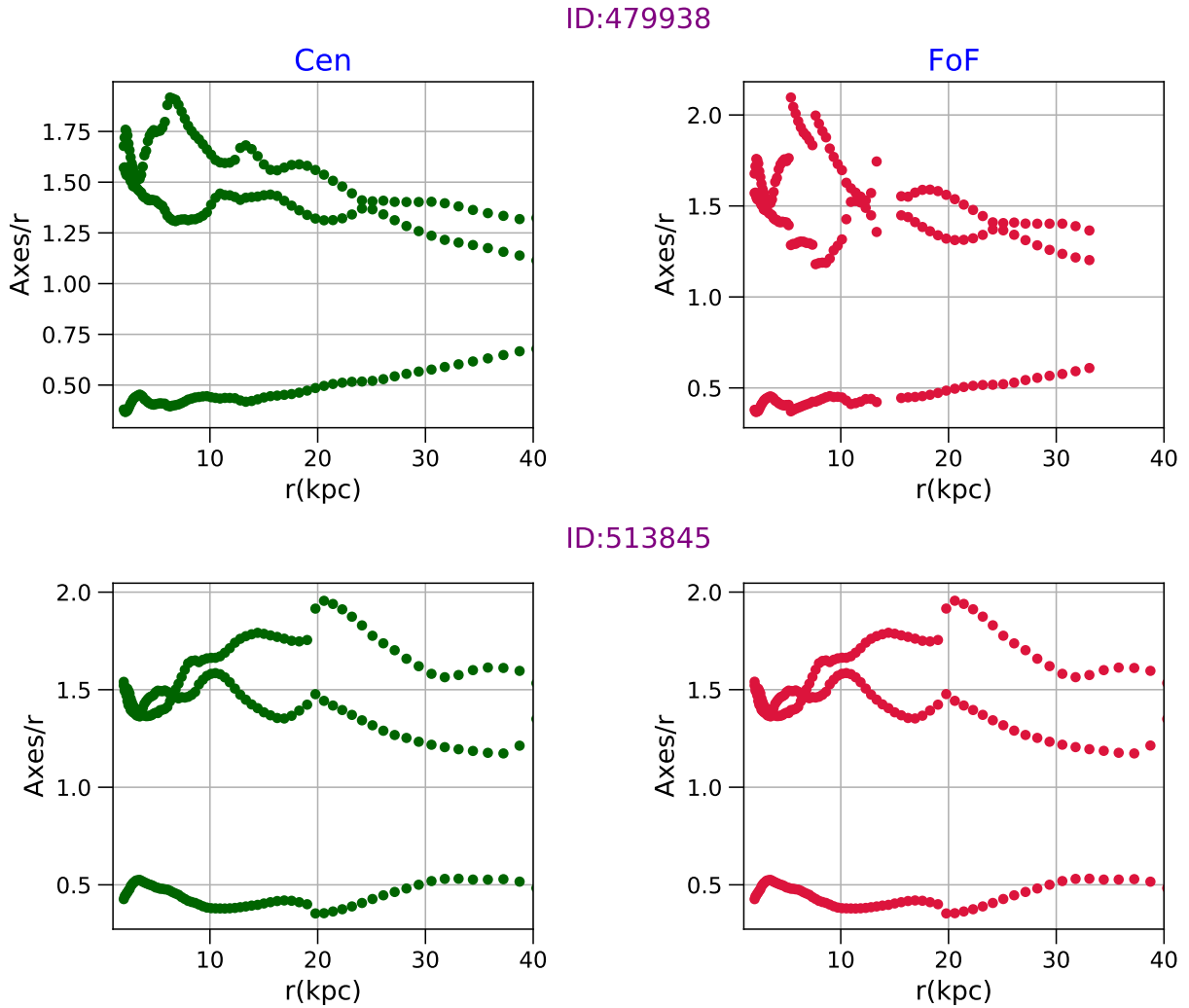
- We made a comparison between the DM ([Emami et al. 2020](#)) and SH shapes using both of EVIM and LSIM for which we computed the  $3 \times 3$  matrix of angles between the min, inter and max eigenvectors in these two methods. The smaller the min-min, inter-inter and max-max angles are, closer the shape of DM and SH would be.



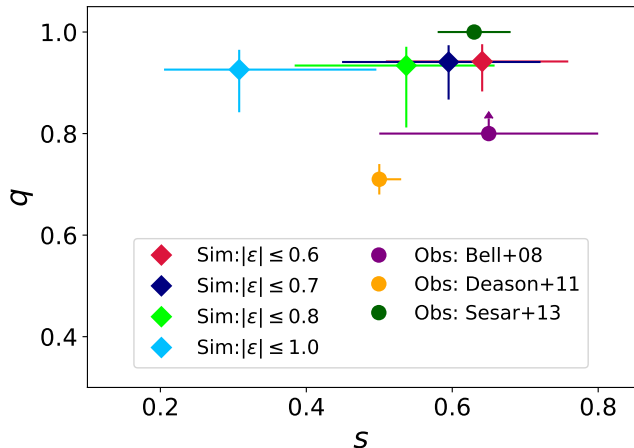
**Figure 14.** Radial profile of  $\varepsilon$  for stars in the central (left), FoF group with no-truncation (middle) and FoF stars truncated above 150 kpc(right) panels. Counter-rotating farther out substructures may dominantly flip the sign of total angular momentum and thus seem to convert the disk structures. They must therefore be removed when we analyze the radial profile of the  $\varepsilon$ .



**Figure 15.** The radial profile of the median and percentile of the shape parameters including the FoF group stars. It is evident that the radial profiles of the median and percentiles of shape parameters are fairly close between the Central(Cen) and substructures(FoF group). This implies that FoF group stars statistically behave the same in shaping the SH as the central stars do.



**Figure 16.** The radial profile of the Axes/ $r$  ratio for two typical halos in our halo sample with (left) and without (right) including the substructures. It is seen that FOF group stars do not change the Axes/ $r$  ratio significantly.



**Figure 17.** Observational constraints on the shape parameters of stellar halo. To fully take the possible impact of the threshold in definition of stellar into account, we add the theoretical constraints from  $\varepsilon \leq (0.6, 0.7, 0.8, 1.0)$ .

- Quite remarkably, based on the EVIM, closer to the center, the angle profiles between the DM and SH are fairly small demonstrating that these two profiles are responding to the baryonic gravitational potential from the stellar disk. However, in some cases, these profiles deviate from each other farther out from the center.

- The inferred angle profile from LSIM, on the other hand, suggest a more oscillating profile. This makes sense as the inferred eigenvalues from LSIM are closer, in the response to the local variations. Therefore, their corresponding eigenvectors reorient more rapidly; owing to the orthogonality at different locations. However, in most cases, it is explicitly seen that while different eigenvalues swing around each other, say inter and max eigenvalues, the angle between inter-inter and inter-max enhances but inter-max and max-inter decreases. This may imply that the halos are close but it was rather hard to exactly track the inter and max eigenvectors very close to the swing location.

- We incorporated the impact of the substructures in the orbital circularity parameter and the shape of stellar halo. Where in the former case, we explicitly showed that in some cases the substructures located farther out from the center might counter rotate with respect to the stars close by and thus including them with no cutoff, may change the distribution of  $\varepsilon$ . Owing to this, it is customary to make a radial cutoff, 150 kpc, and eliminate stars that are farther out from the center while

computing the  $\varepsilon$ . Computing the shape profile using the filtered set of, we showed that the shape of FoF group stars are fairly similar to the central stars.

- Finally, we overlaid our theoretical predictions for the shape parameters on the top of the data from the previous literature. While the shape measurements from our simulations and the observations are not very different, overall, there are differences in detail that might be due to the fact that different observations have taken different tracers and approaches. It is therefore intriguing to make some mock data and make the comparisons with the data more explicitly. This is however left to a future work.

#### DATA AVAILABILITY

The data which are directly related to this publication and figures are available on reasonable request from the corresponding author. The IllustrisTNG simulations themselves are publicly available at [www.tng-project.org/data](http://www.tng-project.org/data) (Nelson et al. 2019). The TNG50 simulation will be made public in the future as well.

#### ACKNOWLEDGEMENT

We warmly acknowledge the very insightful conversations with Sirio Belli, Charlie Conroy, Daniel Eisenstein, Rohan Naidu, Dylan Nelson, Sandro Tacchella, and Annalisa Pillepich for insightful conversation. R.E. thanks the support by the Institute for Theory and Computation (ITC) at the Center for Astrophysics (CFA). We also thank the supercomputer facilities at Harvard university where most of the simulation work was done. MV acknowledges the support through an MIT RSC award, a Kavli Research Investment Fund, NASA ATP grant NNX17AG29G, and NSF grants AST-1814053, AST-1814259 and AST-1909831. SB is supported by the Harvard University through the ITC Fellowship. FM acknowledges the support through the Program "Rita Levi Montalcini" of the Italian MIUR. The TNG50 simulation was realized with computer time granted by Gauss Centre for Supercomputing (GCS) under the GCS Large-Scale Projects GCS-DWAR on GCS share of the supercomputer Hazel Hen at HLRS.

*Software:* h5py (De Buyl et al. 2016), matplotlib (Hunter 2007), numpy (van der Walt et al. 2011), pandas (McKinney Wes et.al), seaborn (Waskom et al. 2020), scipy (Oliphant 2007).

#### REFERENCES

Abadi, M. G., Navarro, J. F., Steinmetz, M., et al. 2003, ApJ, 591, 499. doi:10.1086/375512

Beasley, M. A., Trujillo, I., Leaman, R., et al. 2018, Nature, 555, 483. doi:10.1038/nature25756

- Bell, E. F., Zucker, D. B., Belokurov, V., et al. 2008, *ApJ*, 680, 295
- Belokurov, V., Koposov, S. E., Evans, N. W., et al. 2014, *MNRAS*, 437, 116
- Bird, S. A., Xue, X.-X., Liu, C., et al. 2020, arXiv:2005.05980
- Blumenthal G. R., Faber S. M., Primack J. R., Rees M. J., 1984, *Natur*, 311, 517. doi:10.1038/311517a0
- Bland-Hawthorn, J., & Gerhard, O. 2016, *ARA&A*, 54, 529
- Buck, T., Macciò, A., Ness, M., et al. 2018, *Rediscovering Our Galaxy*, 209
- Buck, T., Obreja, A., Macciò, A. V., et al. 2020, *MNRAS*, 491, 3461
- Conroy, C., Bonaca, A., Cargile, P., et al. 2019, *ApJ*, 883, 107
- Crain, R. A., Schaye, J., Bower, R. G., et al. 2015, *MNRAS*, 450, 1937
- Deason, A. J., Belokurov, V., & Evans, N. W. 2011, *MNRAS*, 416, 2903
- de Buyl, P., Huang, M.-J., & Deprez, L. 2016, arXiv e-prints, arXiv:1608.04904
- El-Badry, K., Quataert, E., Wetzel, A., et al. 2018, *MNRAS*, 473, 1930
- Emami, R., Genel, S., Hernquist, L., et al. 2020, arXiv:2009.09220
- Faccioli, L., Smith, M. C., Yuan, H.-B., et al. 2014, *ApJ*, 788, 105
- Font, A. S., McCarthy, I. G., Poole-Mckenzie, R., et al. 2020, arXiv e-prints, arXiv:2004.01914
- Forbes, D. A., Brodie, J. P., & Grillmair, C. J. 1997, *AJ*, 113, 1652. doi:10.1086/118382
- Garrison-Kimmel, S., Hopkins, P. F., Wetzel, A., et al. 2018, *MNRAS*, 481, 4133
- Genel, S., Vogelsberger, M., Springel, V., et al. 2014, *MNRAS*, 445, 175
- Grand, R. J. J., Helly, J., Fattahi, A., et al. 2018, *MNRAS*, 481, 1726
- Hani, M. H., Ellison, S. L., Sparre, M., et al. 2019, *MNRAS*, 488, 135
- Helmi, A. & White, S. D. M. 1999, *MNRAS*, 307, 495. doi:10.1046/j.1365-8711.1999.02616.x
- Helmi, A., Babusiaux, C., Koppelman, H. H., et al. 2018, *Nature*, 563, 85. doi:10.1038/s41586-018-0625-x
- Hunter, J. D. 2007, *Computing in Science and Engineering*, 9, 90
- Ibata, R. A., Gilmore, G., & Irwin, M. J. 1994, *Nature*, 370, 194. doi:10.1038/370194a0
- Iorio, G. & Belokurov, V. 2019, *MNRAS*, 482, 3868. doi:10.1093/mnras/sty2806
- Iorio, G. & Belokurov, V. 2020, arXiv:2008.02280
- Ivezić, Ž., Sesar, B., Jurić, M., et al. 2008, *ApJ*, 684, 287
- Kado-Fong, E., Greene, J. E., Huang, S., et al. 2020, *ApJ*, 900, 163. doi:10.3847/1538-4357/abacc2
- Mackereth, J. T. & Bovy, J. 2020, *MNRAS*, 492, 3631. doi:10.1093/mnras/staa047
- Marinacci, F., Vogelsberger, M., Pakmor, R., et al. 2018, *MNRAS*, 480, 5113. doi:10.1093/mnras/sty2206
- McKinney, W. et al. *Proceedings of the 9th Python in Science Conference*, 445, 51-56, 2010
- Merritt, A., Pillepich, A., van Dokkum, P., et al. 2020, *MNRAS*, doi:10.1093/mnras/staa1164
- Monachesi, A., Gómez, F. A., Grand, R. J. J., et al. 2016, *MNRAS*, 459, L46
- Monachesi, A., Gómez, F. A., Grand, R. J. J., et al. 2019, *MNRAS*, 485, 2589
- Myeong, G. C., Vasiliev, E., Iorio, G., et al. 2019, *MNRAS*, 488, 1235. doi:10.1093/mnras/stz1770
- Naidu, R. P., Conroy, C., Bonaca, A., et al. 2020, *ApJ*, 901, 48. doi:10.3847/1538-4357/abaef4
- Naiman, J. P., Pillepich, A., Springel, V., et al. 2018, *MNRAS*, 477, 1206
- Navarro, J. F., Frenk, C. S., & White, S. D. M. 1997, *ApJ*, 490, 493. doi:10.1086/304888
- Nelson, D., Pillepich, A., Springel, V., et al. 2018, *MNRAS*, 475, 624. doi:10.1093/mnras/stx3040
- Nelson, D., Pillepich, A., Springel, V., et al. 2019, *MNRAS*, 490, 3234. doi:10.1093/mnras/stz2306
- Nelson, D., Springel, V., Pillepich, A., et al. 2019, *Computational Astrophysics and Cosmology*, 6, 2
- Oliphant, T. E. 2007, *Computing in Science and Engineering*, 9, 10
- Orr, M. E., Hayward, C. C., Medling, A. M., et al. 2019, arXiv e-prints, arXiv:1911.00020
- Oser, L., Ostriker, J. P., Naab, T., et al. 2010, *ApJ*, 725, 2312. doi:10.1088/0004-637X/725/2/2312
- Pillepich, A., Springel, V., Nelson, D., et al. 2018, *MNRAS*, 473, 4077
- Pillepich, A., Nelson, D., Hernquist, L., et al. 2018, *MNRAS*, 475, 648. doi:10.1093/mnras/stx3112
- Pillepich, A., Nelson, D., Springel, V., et al. 2019, *MNRAS*, 490, 3196
- Planck Collaboration, Ade, P. A. R., Aghanim, N., et al. 2016, *A&A*, 594, A13
- Posti, L., & Helmi, A. 2019, *A&A*, 621, A56
- Sanderson, R. E., Wetzel, A., Loebman, S., et al. 2020, *ApJS*, 246, 6
- Santistevan, I. B., Wetzel, A., El-Badry, K., et al. 2020, arXiv e-prints, arXiv:2001.03178
- Schaye, J., Crain, R. A., Bower, R. G., et al. 2015, *MNRAS*, 446, 521

- Schinnerer, E., Meidt, S. E., Pety, J., et al. 2013, *ApJ*, 779, 42
- Schulze, F., Remus, R.-S., Dolag, K., et al. 2020, *MNRAS*, 493, 3778
- Searle, L. & Zinn, R. 1978, *ApJ*, 225, 357.  
doi:10.1086/156499
- Sesar, B., Ivezić, Ž., Grammer, S. H., et al. 2010, *ApJ*, 708, 717
- Sesar, B., Ivezić, Ž., Stuart, J. S., et al. 2013, *AJ*, 146, 21
- Sijacki, D., Vogelsberger, M., Genel, S., et al. 2015, *MNRAS*, 452, 575
- Springel, V. 2010, *MNRAS*, 401, 791
- Springel, V., Pakmor, R., Pillepich, A., et al. 2018, *MNRAS*, 475, 676. doi:10.1093/mnras/stx3304
- Trayford, J. W., Frenk, C. S., Theuns, T., et al. 2019, *MNRAS*, 483, 744
- Van der Walt, S., Colbert, S. C., & Varoquaux, G. 2011, *Computing in Science and Engineering*, 13, 22
- Vivas, A. K., & Zinn, R. 2006, *AJ*, 132, 714
- Vogelsberger, M., Genel, S., Springel, V., et al. 2014, *MNRAS*, 444, 1518
- Vogelsberger, M., Genel, S., Springel, V., et al. 2014, *Nature*, 509, 177
- Vogelsberger, M., Marinacci, F., Torrey, P., et al. 2020, *Nature Reviews Physics*, 2, 42
- Waskom, M., Botvinnik, O., Ostblom, J., et al. 2020, *mwaskom/seaborn: v0.10.0 (January 2020)*, v0.10.0, Zenodo, doi:10.5281/zenodo.3629446
- Watkins, L. L., Evans, N. W., Belokurov, V., et al. 2009, *MNRAS*, 398, 1757
- Weinberger, R., Springel, V., Hernquist, L., et al. 2017, *MNRAS*, 465, 3291
- White, S. D. M. & Rees, M. J. 1978, *MNRAS*, 183, 341.  
doi:10.1093/mnras/183.3.341
- White, S. D. M. & Frenk, C. S. 1991, *ApJ*, 379, 52.  
doi:10.1086/170483

## APPENDIX

## A. HALO CLASSIFICATION

As already specified in the main body of paper, we may put the stellar halo shape in 2 main categories: twisted halos and twisted-stretched halos. While we present very few cases in the text, to make the picture clearer, here we present the radial profile of Axes/ $r$  ratio, angle of the min-inter-max eigenvectors with few fixed vectors and also the radial profile of the shape parameters  $(s, q)$  for the entire of 25 galaxies in our sample. Also, to have an unambiguous association of angles at initial points, we demand that all of angles are initially less than 90 deg.

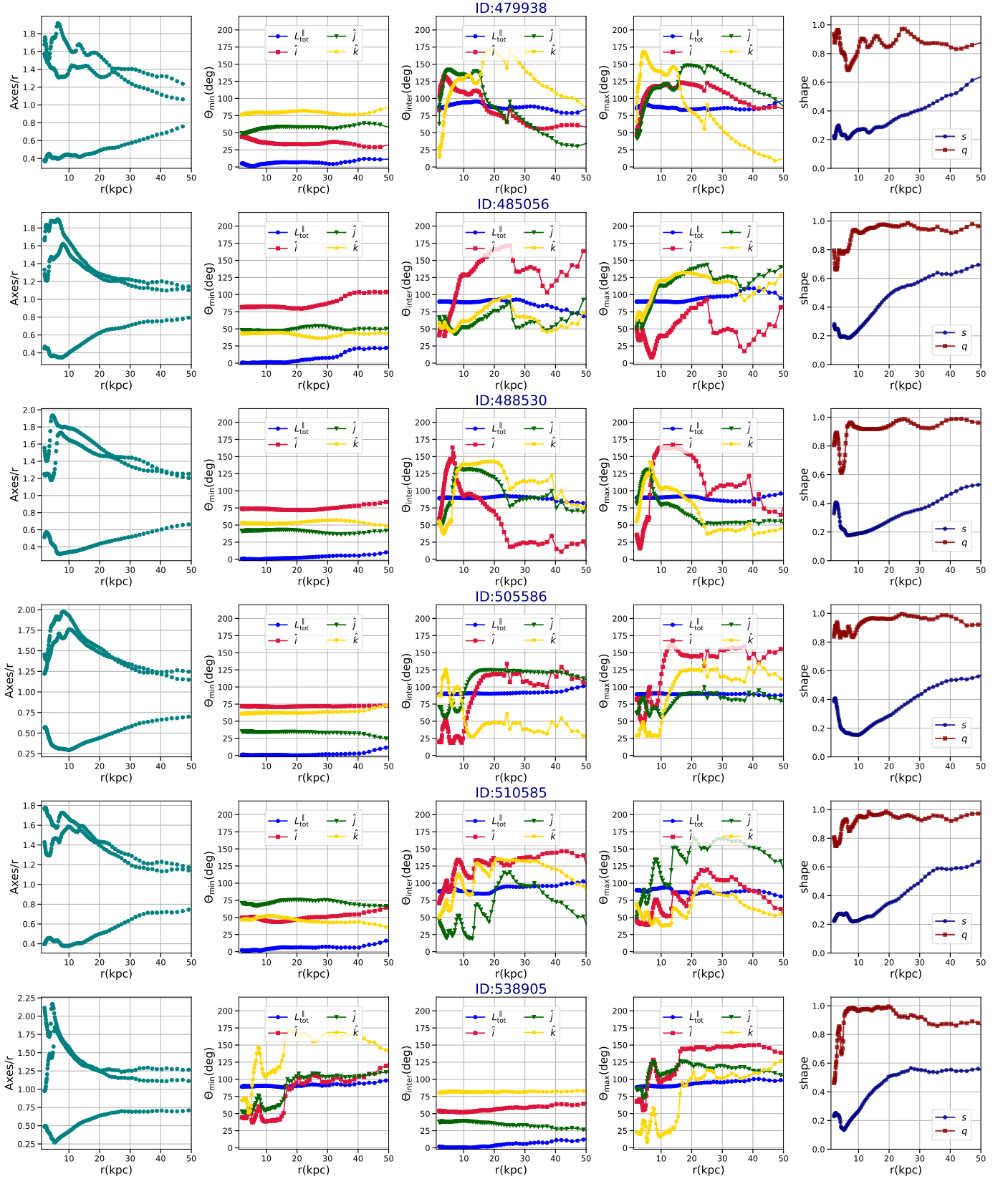
A.1. *Twisted halos*

First, we present the population of twisted halos. There are in total 13 twisted halos in our sample. Figures 18 and 19 present this class of halos. We have truncated the radial profile up to where there are some collection of points for which the shape finder algorithm does not converge. For example, while the presented halos in Figure 18 are converged around(above) 50 kpc, halos associated with Figure 19 are mostly converged until 30 kpc continuously and have gaps in between for larger radii. Owing to this, we truncate their shape profile at around 25-30 kpc.

A.2. *Twisted-Stretched halos*

Next, we display twisted-stretched halos, as defined in the main text. There are in total 12 halos in this class. Figures 20 and 21 present the halos in this class. In a manner similar to the twisted halos, here we truncate the radial profile until where we see some gaps in the collection of the converged points.

## Twisted Halos(1)

Figure 18. The radial profile of Axes/ $r$ , angles and shape parameters for the twisted halos.

## Twisted Halos(2)

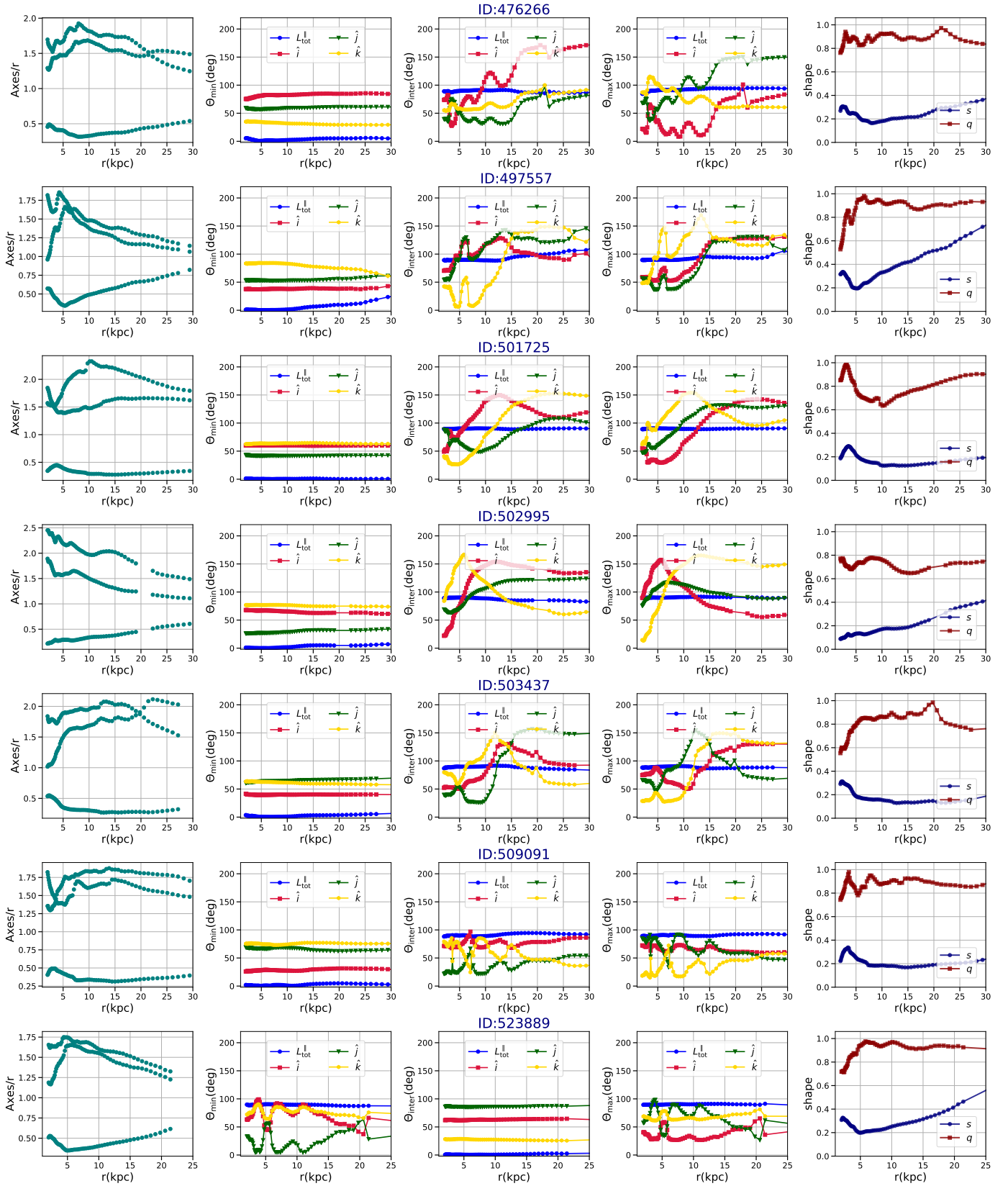


Figure 19. The radial profile of Axes/ $r$ , angles and shape parameters for the twisted halos.

## Twisted-Stretched Halos(1)

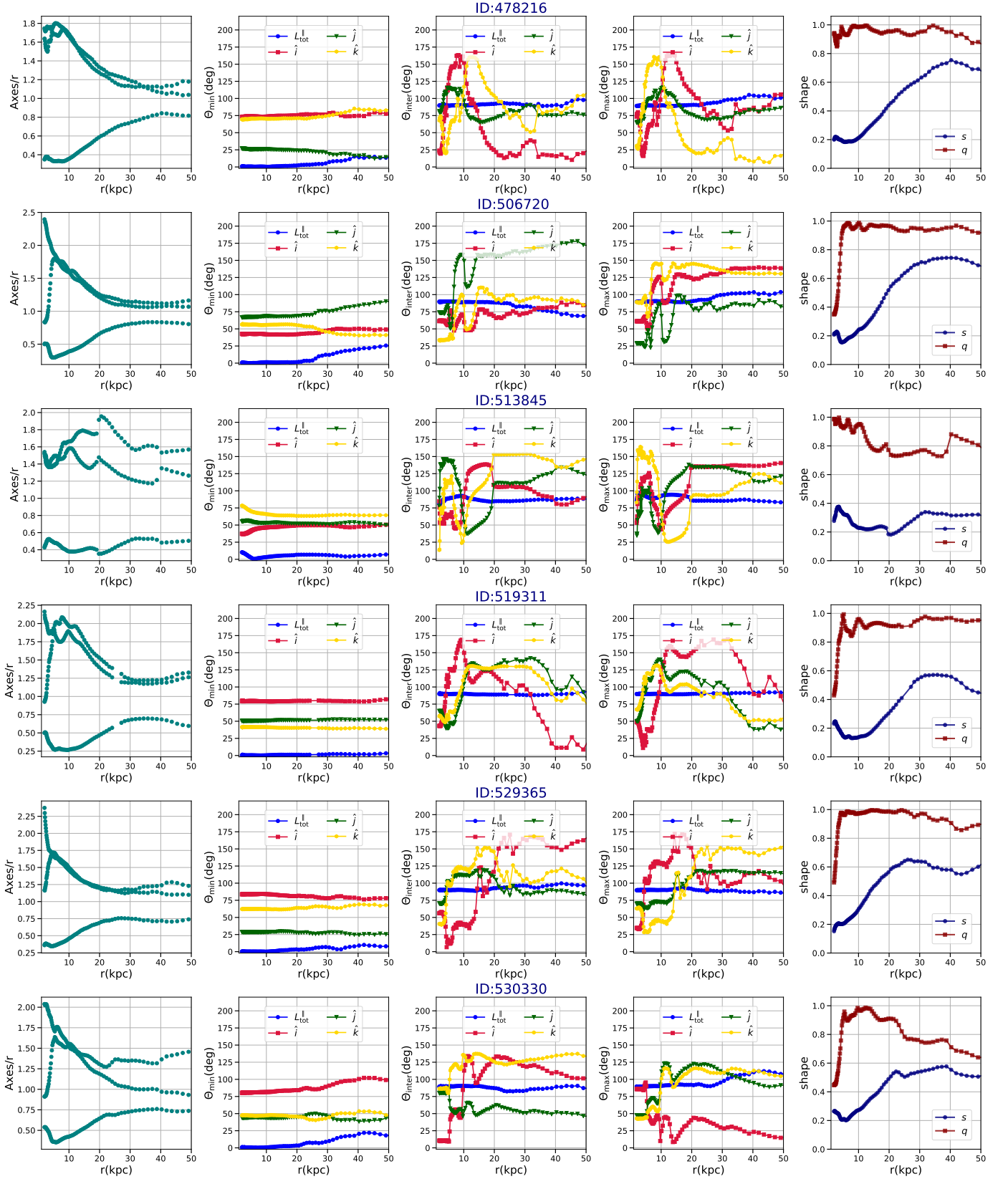


Figure 20. The radial profile of Axes/ $r$ , angles and shape parameters for the twisted-stretched halos.

## Twisted-Stretched Halos(2)

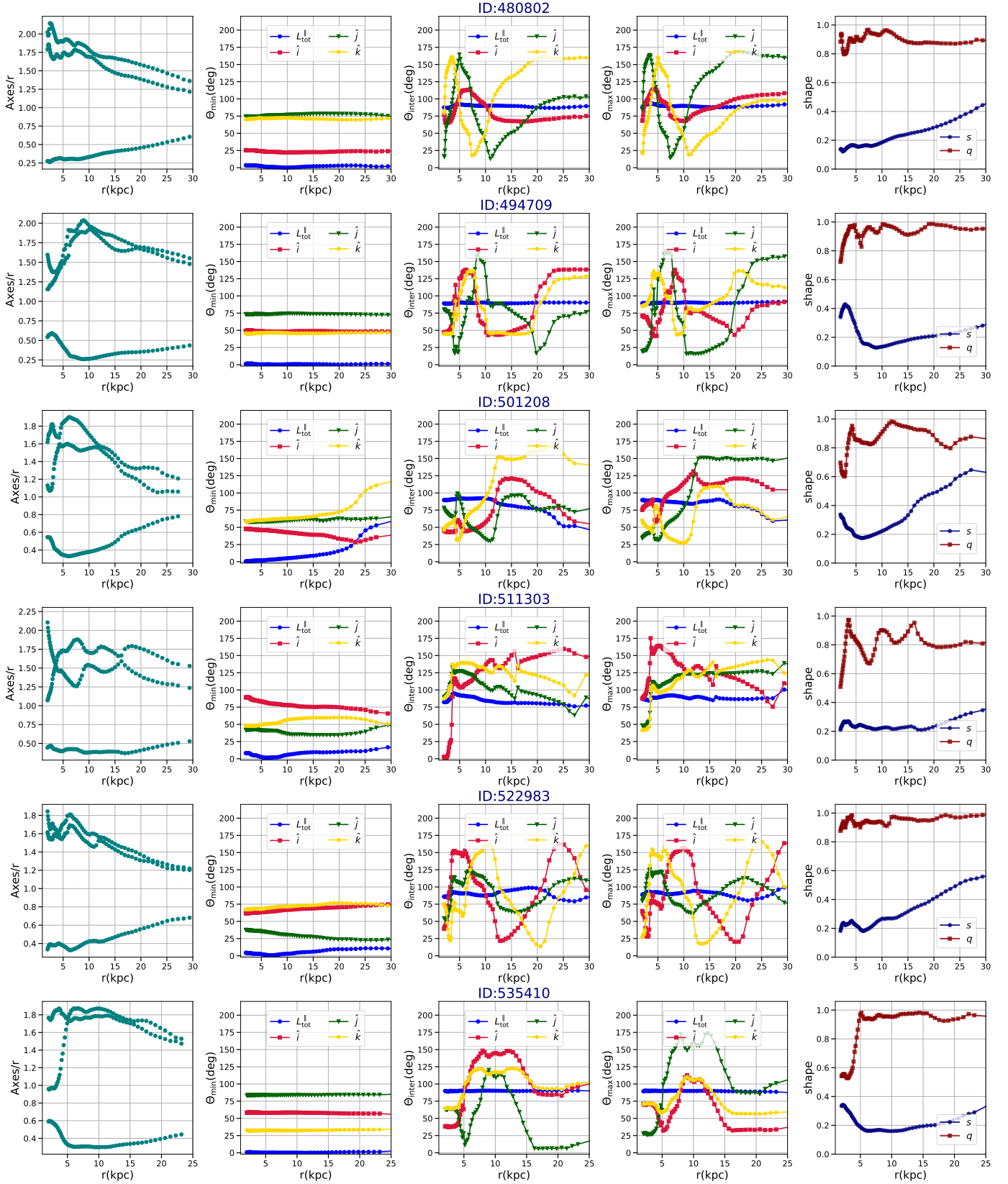


Figure 21. The radial profile of Axes/ $r$ , angles and shape parameters for the twisted-stretched halos.